

# A PKA inhibitor motif within SMOOTHENED controls Hedgehog signal transduction

Received: 1 July 2021

Accepted: 22 August 2022

Published online: 06 October 2022

 Check for updates

John T. Happ<sup>1,12</sup>, Corvin D. Arveseth<sup>1,10,12</sup>, Jessica Bruystens<sup>2,12</sup>, Daniela Bertinetti<sup>3,12</sup>, Isaac B. Nelson<sup>1,12</sup>, Cristina Olivieri<sup>4,12</sup>, Jingyi Zhang<sup>5</sup>, Danielle S. Hedeem<sup>1</sup>, Ju-Fen Zhu<sup>1</sup>, Jacob L. Capener<sup>1,11</sup>, Jan W. Bröckel<sup>3</sup>, Lily Vu<sup>6</sup>, C. C. King<sup>2,7</sup>, Victor L. Ruiz-Perez<sup>8,9</sup>, Xuecai Ge<sup>5</sup>, Gianluigi Veglia<sup>1,4</sup>, Friedrich W. Herberg<sup>3</sup>, Susan S. Taylor<sup>2,7</sup>✉ and Benjamin R. Myers<sup>1</sup>✉

The Hedgehog (Hh) cascade is central to development, tissue homeostasis and cancer. A pivotal step in Hh signal transduction is the activation of glioma-associated (GLI) transcription factors by the atypical G protein-coupled receptor (GPCR) SMOOTHENED (SMO). How SMO activates GLI remains unclear. Here we show that SMO uses a decoy substrate sequence to physically block the active site of the cAMP-dependent protein kinase (PKA) catalytic subunit (PKA-C) and extinguish its enzymatic activity. As a result, GLI is released from phosphorylation-induced inhibition. Using a combination of in vitro, cellular and organismal models, we demonstrate that interfering with SMO-PKA pseudosubstrate interactions prevents Hh signal transduction. The mechanism uncovered echoes one used by the Wnt cascade, revealing an unexpected similarity in how these two essential developmental and cancer pathways signal intracellularly. More broadly, our findings define a mode of GPCR-PKA communication that may be harnessed by a range of membrane receptors and kinases.

The Hh signaling cascade is fundamental to embryogenesis, controlling the development of nearly every vertebrate organ<sup>1–4</sup>. Insufficient Hh pathway activity underlies birth defects affecting the nervous, cardiovascular and musculoskeletal systems<sup>5–7</sup>. On the other hand, Hh pathway overactivation drives several common cancers, including basal cell carcinoma of the skin (the most common cancer in North America) and medulloblastoma (the most common pediatric brain tumor)<sup>8,9</sup>.

The Hh pathway uses an unusual signal transduction mechanism involving layers of repressive interactions<sup>1–4</sup>. In the pathway ‘off’

state, PKA-C phosphorylates glioma-associated (GLI) transcription factor, stimulating its proteolysis into a truncated transcriptional repressor that inhibits target gene expression<sup>4,10</sup>. In the pathway ‘on’ state, Hh ligands bind to and inactivate the 12-transmembrane sterol transporter PATCHED1 (PTCH1), which releases SMOOTHENED (SMO) from PTCH1-mediated inhibition<sup>4</sup>. This process allows SMO to access its endogenous sterol ligands and undergo an activating conformational change<sup>11–14</sup>. Once activated, SMO blocks PKA-C-mediated phosphorylation of GLI<sup>15–18</sup>, a key step that likely occurs within a solitary

<sup>1</sup>Department of Oncological Sciences, Department of Biochemistry, and Department of Bioengineering, University of Utah School of Medicine, Salt Lake City, UT, USA. <sup>2</sup>Department of Pharmacology, University of California, San Diego, La Jolla, CA, USA. <sup>3</sup>Institute for Biology, Department of Biochemistry, University of Kassel, Kassel, Germany. <sup>4</sup>Department of Biochemistry, Molecular Biology, and Biophysics, University of Minnesota, Minneapolis, MN, USA. <sup>5</sup>Department of Molecular and Cell Biology, School of Natural Sciences, University of California, Merced, CA, USA. <sup>6</sup>Department of Neurobiology, University of California, San Diego, La Jolla, CA, USA. <sup>7</sup>Department of Chemistry and Biochemistry, University of California, San Diego, La Jolla, CA, USA. <sup>8</sup>Instituto de Investigaciones Biomédicas ‘Alberto Sols’, Consejo Superior de Investigaciones Científicas (CSIC), Universidad Autónoma de Madrid, Madrid, Spain. <sup>9</sup>CIBER de Enfermedades Raras (CIBERER), Instituto de Salud Carlos III (ISCIII), Madrid, Spain. <sup>10</sup>Present address: Washington University School of Medicine, St. Louis, MO, USA. <sup>11</sup>Present address: Biological and Biomedical Sciences Program, University of North Carolina, Chapel Hill, NC, USA. <sup>12</sup>These authors contributed equally: John T. Happ, Corvin D. Arveseth, Jessica Bruystens, Daniela Bertinetti, Isaac B. Nelson, Cristina Olivieri.

✉e-mail: [staylor@ucsd.edu](mailto:staylor@ucsd.edu); [benjamin.myers@hci.utah.edu](mailto:benjamin.myers@hci.utah.edu)

microtubule-based organelle known as the primary cilium<sup>19–21</sup>. This tiny cell-surface compartment is thought to facilitate the essential protein-protein interactions and biochemical reactions in the Hh pathway, owing to its high surface-area-to-volume ratio, compartmentalized structure and unique protein and lipid repertoire. Following the loss of PKA-C-mediated phosphorylation, GLI becomes activated and consequently controls the expression of proliferative or differentiative genes<sup>10</sup>. SMO regulation of PKA-C is thus a critical event in transducing Hh signals from the cell surface to the nucleus. However, the underlying mechanism has remained mysterious for decades<sup>1–4</sup>.

G protein-coupled receptors (GPCRs) classically inhibit PKA-C via well-characterized signaling cascades involving heterotrimeric G protein-mediated effects on cAMP. Lowering cAMP reduces PKA-C activity, either by promoting interactions with PKA regulatory (PKA-R) subunits to form inactive PKA holoenzymes<sup>22–24</sup> or by affecting the conformational states of preformed PKA-C–PKA-R complexes<sup>25–28</sup>. In contrast, we recently found that SMO prevents PKA-C from phosphorylating substrates via a noncanonical mechanism. SMO directly interacts with PKA-C subunits, recruiting them to the ciliary membrane and thereby restricting their access to soluble GLI proteins. SMO–PKA-C interactions are triggered by GPCR kinases 2 and 3 (GRK2/3), which recognize the SMO active state and phosphorylate the cytoplasmic tail (C-tail) of SMO to promote PKA-C binding. Based on these observations, we proposed that active, phosphorylated SMO binds to and sequesters PKA-C within the cilium, which prevents phosphorylation of GLI and thereby promotes GLI activation<sup>29</sup>.

Here we uncover a critical and unexpected component of the SMO–PKA-C regulatory mechanism in which SMO physically blocks PKA-C enzymatic activity. We show that the SMO proximal C-tail (pCT) acts as a decoy PKA-C substrate that binds to and occludes the kinase active site, thereby preventing phosphorylation of PKA-C targets. Our findings with SMO thus demonstrate that GPCRs can function as direct PKA-C inhibitors. However, this decoy substrate mechanism appears to apply more generally to transmembrane receptors and kinases in other signaling pathways.

## Results

### SMO binds and inhibits PKA-C as a pseudosubstrate

The principal regulators of PKA-C activity within cells are PKA-R subunits<sup>30</sup> and the heat-stable protein kinase inhibitor (PKI) proteins<sup>31</sup>. PKI proteins and type I (PKA-RI) regulatory subunits operate as pseudosubstrates that bind within the PKA-C active site but cannot undergo phosphorylation. As a result, the enzyme's phosphoryl transfer and substrate turnover cycle is interrupted<sup>30–33</sup>. PKA-R/PKA-C holoenzymes dissociate on cAMP binding to PKA-R, releasing catalytically active PKA-C<sup>30</sup>. In contrast, PKI proteins interact with PKA-C independently of cAMP levels<sup>31</sup>. Despite their divergent regulatory influences, PKI and PKA-RI engage the PKA-C active site cleft using similar sequence motifs<sup>30,33</sup>.

Inspection of the mouse SMO sequence revealed a region within the pCT (residues 615–638) that bears the hallmarks of a PKA-C pseudosubstrate (Fig. 1a). First, in contrast to canonical PKA-C substrates, which contain a serine or threonine at a canonical phosphorylation site (P site)<sup>34</sup>, SMO possesses a nonphosphorylatable residue, alanine, at this position. Second, SMO contains arginines at the P-2 and P-3 positions that are essential in other pseudosubstrates (PKI and PKA-RI) for binding the PKA-C active site<sup>35–38</sup>. Third, SMO contains a hydrophobic residue, isoleucine, at P + 1 and a bulkier aromatic residue, tryptophan, at P-13, both of which contribute to high-affinity PKI interactions with PKA-C<sup>39–41</sup>. Finally, SMO harbors a predicted  $\alpha$ -helical sequence N terminal to the pseudosubstrate region (Fig. 1a), resembling a domain in PKI that is required for high-affinity interactions with PKA-C<sup>42,43</sup>. Based on these observations and the studies described below, we refer to SMO residues 615–638 as the 'SMO PKI motif'.

We hypothesized that SMO uses its PKI motif as a pseudosubstrate to bind and inhibit PKA-C, thereby activating GLI. Consistent with this

hypothesis, residues 615–637 of mouse SMO are essential for communication with GLI<sup>44</sup>, although the structure, function and interacting partner(s) of this SMO region are all undefined. Furthermore, the P, P + 1, P-2, P-3 and P-13 residues critical for PKA-C pseudosubstrate function in bona fide PKI proteins are highly conserved among SMO orthologs (Extended Data Fig. 1), suggestive of a central role in SMO functionality.

We measured the affinity of the SMO PKI motif for PKA-C $\alpha$ , the best-studied and most ubiquitously expressed PKA-C isoform<sup>32</sup>, using fluorescence polarization assays. A fluorescently labeled peptide encompassing the SMO PKI motif (standard SMO peptide, Fig. 1a, red) bound saturably to purified human ( $K_D = 823$  nM, Fig. 1b (top)) or mouse ( $K_D = 911$  nM, Extended Data Fig. 2a (left)) PKA-C $\alpha$ . These interactions showed pseudosubstrate characteristics: they were strongly ATP-dependent<sup>45</sup> ( $EC_{50}$  for ATP = 19.2  $\mu$ M (human) or 0.59  $\mu$ M (mouse), Fig. 1b (bottom) and Extended Data Fig. 2a (right)) and were blocked by alanine substitution of the P-2/P-3 arginines and the P-13 tryptophan, hereafter referred to as the 'WRR mutation' (Fig. 1c and Extended Data Fig. 2b). Along similar lines, direct surface plasmon resonance (SPR) binding studies revealed that a recombinant protein encompassing the entire 93 amino-acid SMO pCT bound specifically to mouse PKA-C $\alpha$  (Fig. 1d). These interactions displayed fast on- and off-rates with transient kinetics, and steady-state analysis of the binding data revealed a  $K_D$  of 752 nM (Extended Data Fig. 2c,d). Consistent with our peptide-binding studies, PKA-C interactions with the SMO pCT depended strictly on ATP and  $MgCl_2$  (Extended Data Fig. 2e), and no PKA-C binding was observed for the WRR mutant (Fig. 1e and Extended Data Fig. 2c,e). The above SMO PKI binding assays revealed weaker interactions with PKA-C than observed for conventional pseudosubstrates ( $K_D = 1.1$  nM for PKI $\alpha$ (5–24) peptide<sup>46</sup>). We discuss the biochemical basis and biological importance of these affinity differences below.

We next studied the interaction between PKA-C and the SMO PKI motif at the atomic level using nuclear magnetic resonance (NMR) spectroscopy. Binding of a peptide encompassing the SMO PKI motif induced chemical shift perturbations (CSP) in the amide fingerprint of the enzyme, especially within key domains throughout the PKA-C kinase core (Fig. 2a and Extended Data Figs. 3–5). The SMO peptide CSPs reflect specific effects on PKA-C, based on several lines of evidence. First, the CSPs involve regions throughout the kinase N-lobe critical for pseudosubstrate peptide binding and subsequent reorientation of the kinase domain, such as the  $\alpha$ A,  $\alpha$ F and  $\alpha$ G helices as well as the catalytic loop (Fig. 2a,b). Second, a SMO peptide harboring the WRR mutation displayed consistently smaller CSPs than its wild-type counterpart, particularly in the kinase N-lobe including the peptide-binding groove (Fig. 2a and Extended Data Fig. 4). Third, several of the SMO peptide CSPs exhibit a linear dependence on SMO peptide concentration (Extended Data Fig. 3), indicative of a specific interaction with the kinase. Finally, PKI $\alpha$ (5–24) readily displaced the SMO peptide when added as a competitor in our NMR samples, demonstrating that both peptides compete for overlapping sites within the PKA-C peptide-binding groove (Fig. 2c and Extended Data Fig. 5). Thus, the SMO peptide biases the kinase toward an inactive conformation, although to a lesser extent than does PKI $\alpha$ (5–24). This conclusion is consistent with the divergent biological functions and regulatory mechanisms of PKI versus SMO (Discussion).

SMO PKI peptides also blocked PKA-C enzymatic activity *in vitro*, as assessed via a PKA-C substrate phosphorylation assay<sup>47</sup>, with an extended length peptide (Fig. 1a) inhibiting PKA-C more profoundly (Fig. 3a). In keeping with this trend, the recombinant SMO pCT (Supplementary Fig. 1a,b) required 5–10-fold lower concentrations to efficiently block PKA-C activity compared to SMO PKI peptides (half-maximum inhibitory concentration ( $IC_{50}$ ) of 10.9  $\mu$ M for pCT versus 50–125  $\mu$ M for SMO PKI peptides, Fig. 3b). Consistent with a pseudosubstrate mode of inhibition, introducing the WRR mutation into the SMO pCT restored PKA-C activity (Fig. 3c). These data

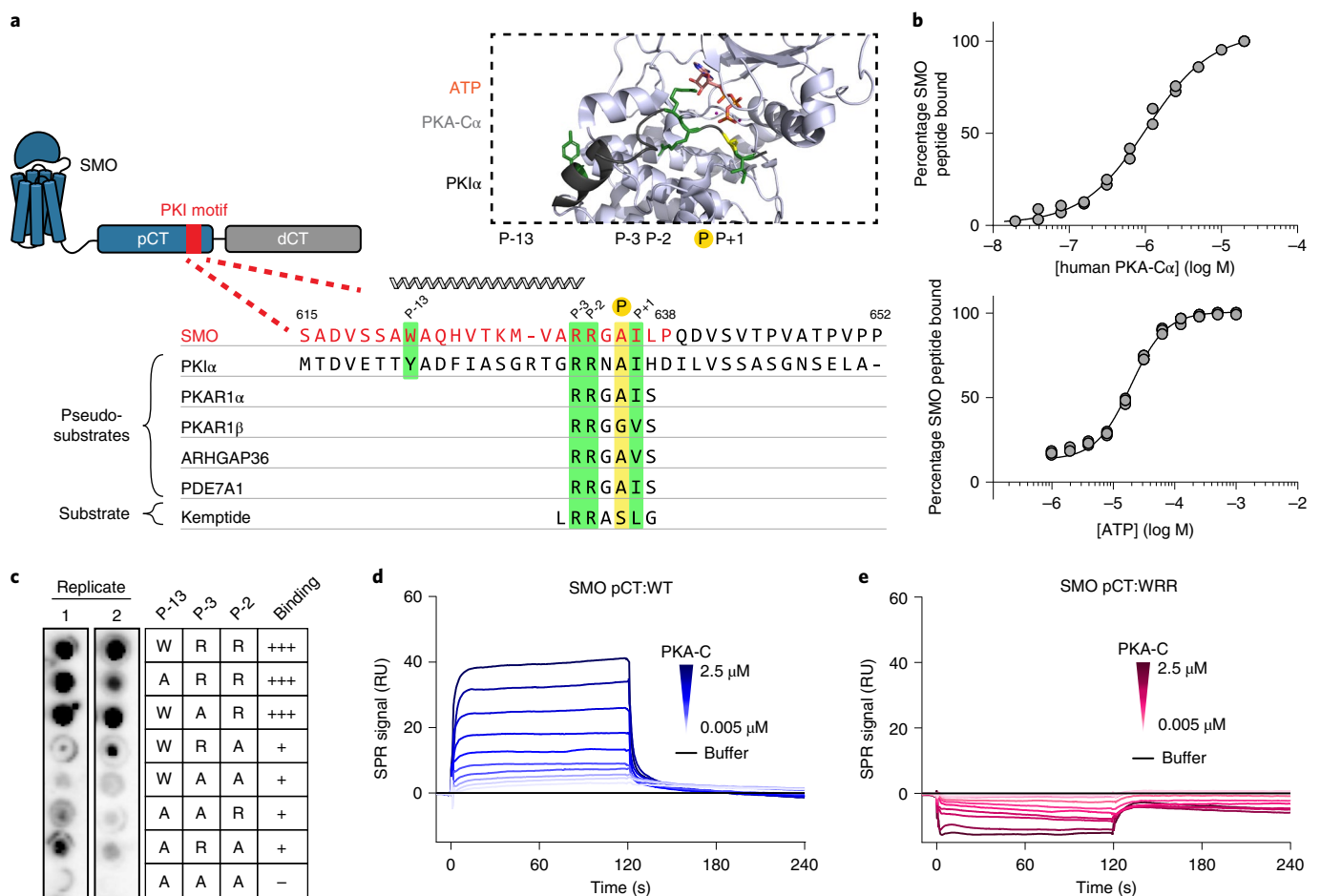


**Fig. 1 | SMO binds PKA-C as a pseudosubstrate.** **a**, CLUSTAL alignment of the mouse SMO pCT with the PKI $\alpha$  pseudosubstrate region. Additional PKA-C pseudosubstrate and substrate sequences are provided for comparison<sup>32,65,98</sup>. The P site is yellow, other key conserved residues are green. Spiral cartoon above the alignment indicates the predicted SMO helical region. Standard (615–638) and extended (615–652) SMO peptides used for in vitro assays are colored red or black, respectively. Inset shows the structure of PKA-C $\alpha$  bound to PKI $\alpha$ (5–24) (PDB 3FJQ), with ATP colored orange and key PKI residues colored as described above. **b**, Top, fluorescence polarization assay using FAM-labeled SMO peptide, 1 mM ATP and varying concentrations of human PKA-C $\alpha$ . Points represent the

mean from two separate experiments composed of quadruplicates. Bottom, the same assay except with 3  $\mu$ M PKA-C $\alpha$  and varying concentrations of ATP. Quadruplicates representative of two independent trials are plotted. **c**, Overlay of purified mouse PKA-C $\alpha$  onto an array of SMO peptides containing the indicated substitutions in the P-13, P-3 and P-2 positions. **d**, SPR sensorgram for binding of PKA-C $\alpha$ , in concentrations ranging from 5 nM to 2.5  $\mu$ M, to GST-tagged wild-type (WT) SMO pCT. Buffer contained 1 mM ATP and 10 mM MgCl $_2$ . **e**, As **d**, but with SMO pCT harboring the WRR mutation. Note that the negative signal results from the subtraction of the nonspecific binding of PKA-C $\alpha$  to a GST control surface.

indicate that the SMO PKI motif is sufficient to inhibit PKA-C substrate phosphorylation, with additional sequences in the pCT enhancing the efficiency of inhibition.

### The SMO PKI motif is required for Hh signal transduction

We next asked whether the SMO PKI motif contributes to PKA-C binding and inhibition in living systems. Our initial studies involved a simplified human embryonic kidney 293 (HEK293) cell model for SMO-PKA-C regulation and used truncated SMO constructs (either SMO657 or SMO674, with the number indicating the C terminal-most residue) that exhibit improved expression and biochemical stability compared to full-length SMO<sup>29</sup>. We used bioluminescence resonance energy transfer (BRET)<sup>48,49</sup> to detect interactions between nanoluciferase (nanoluc)-tagged SMO and yellow fluorescent protein- (YFP-) tagged PKA-C constructs in a cellular environment<sup>29</sup>. In this assay, PKA-C exhibited strong, specific BRET with wild-type SMO657, but not with SMO657 harboring the WRR mutation (Fig. 4a). Coimmunoprecipitation assays confirmed these results (Extended Data Fig. 6a). Similarly, the WRR mutation prevented SMO674 from colocalizing

with PKA-C at the plasma membrane<sup>29</sup>, as determined by live-cell confocal microscopy (Fig. 4b).

We extended the above findings to more physiological cellular models of Hh signaling in primary cilia, using SMO constructs with full-length unmodified C termini. We studied SMO-PKA-C colocalization in cilia using inner medullary collecting duct (IMCD3) cells, a robustly ciliated kidney cell line that is used extensively in studies of ciliary Hh signal transduction<sup>29,50–52</sup>. On Hh pathway activation, SMO accumulates in IMCD3 primary cilia<sup>50–52</sup>, where it colocalizes with PKA-C<sup>29</sup>. In contrast, PKA-C displayed dramatically reduced colocalization in cilia with SMO containing the WRR mutation (Extended Data Fig. 6b). The WRR mutation also prevented interaction between SMO and PKA-C (expressed at near-endogenous levels<sup>29</sup>) in these ciliated cells (Fig. 4c). We also observed that SMO colocalizes with endogenous PKA-C in the primary cilium of NIH3T3 fibroblasts (Fig. 5 and Extended Data Fig. 7), another widely used cultured cell model of Hh signal transduction. Colocalization only occurred when SMO was in an active, agonist-bound state; it did not occur when SMO was bound to the inverse agonist cyclopamine (Fig. 5), which induces SMO to

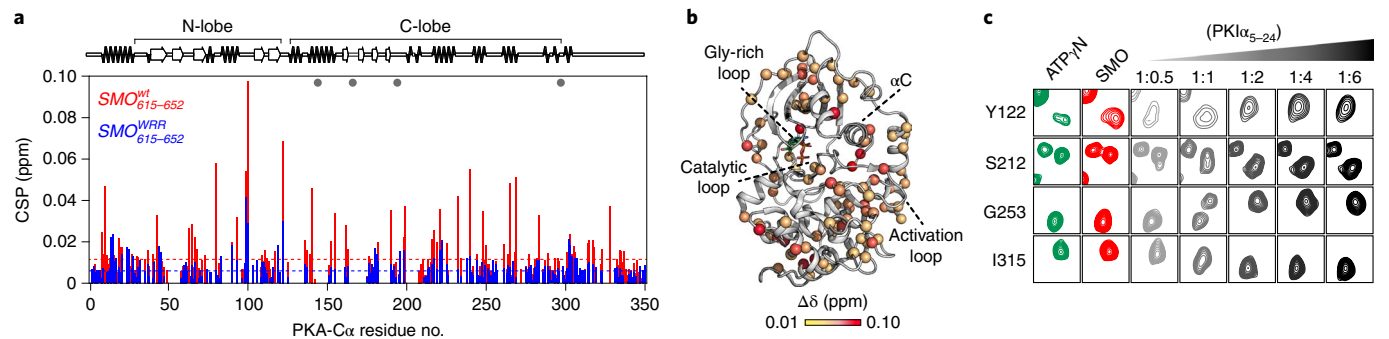


**Fig. 2 | SMO induces changes in the amide fingerprint of PKA-C.** **a**, Mapping of amide backbone CSP for [<sup>1</sup>H, <sup>15</sup>N]-labeled PKA-C $\alpha$  bound to nucleotide (ATP $\gamma$ N) and either an extended SMO wild-type (red) or WRR mutant (blue) peptide, provided at a 1:6 PKA-C $\alpha$ :peptide ratio and calculated relative to ATP $\gamma$ N-bound PKA-C $\alpha$  without peptide. Key secondary structural elements within the N-lobe and C-lobe of PKA-C $\alpha$  are determined via assignment of resonances in the kinase spectrum as previously described<sup>43</sup>, and are indicated along the x axis. Gray spheres designate PKA-C $\alpha$  residues that typically show a signal for

PKI $\alpha$ (5–24)<sup>43,99,100</sup> but are broadened out on binding SMO. Dashed lines indicate one standard deviation from baseline for each dataset. **b**, CSP values from **a** were mapped onto the PKA-C $\alpha$  structure (PDB 4WB5) and displayed as a heatmap. **c**, Competition-induced changes in the indicated residues observed in the NMR spectrum on titration of PKI $\alpha$ (5–24) peptide (1:0.5, 1:1, 1:2, 1:4 or 1:6 ratios, relative to PKA-C $\alpha$ ) into a SMO peptide–ATP $\gamma$ N–PKA-C $\alpha$  complex (1:6 PKA-C $\alpha$ :SMO peptide ratio). Spectrum for ATP $\gamma$ N-bound PKA-C $\alpha$  (green) and SMO peptide–ATP $\gamma$ N–PKA-C $\alpha$  complex (red) are shown for reference.

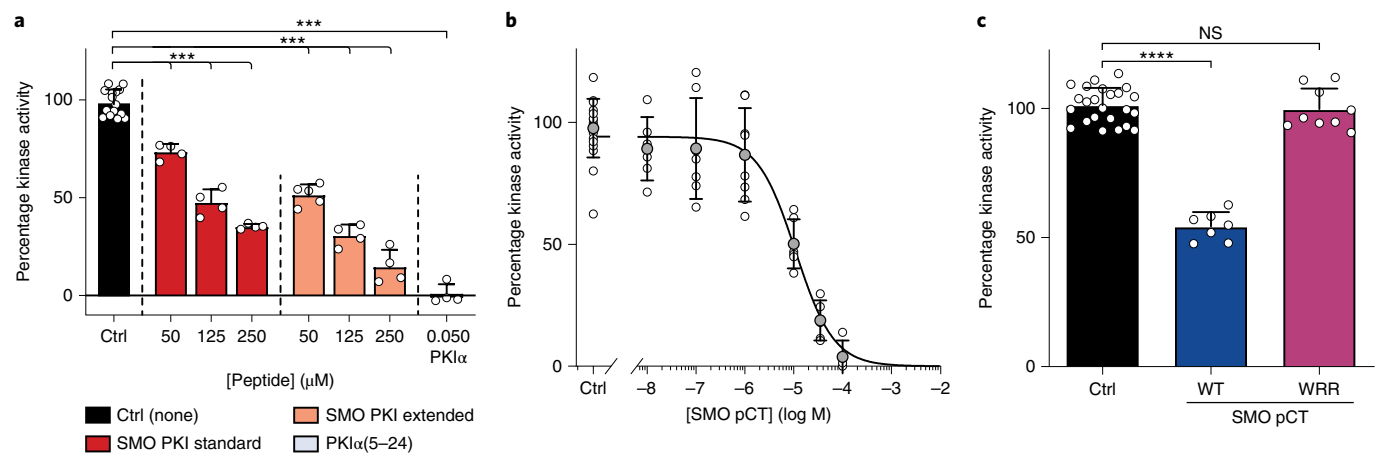


**Fig. 3 | SMO inhibits PKA-C enzymatic activity.** **a**, Spectrophotometric assay of PKA-C $\alpha$  substrate phosphorylation, in the presence of standard (red) or extended (coral) SMO peptides (Fig. 1a) or a control PKI $\alpha$ (5–24) peptide (gray). **b**, Concentration-dependent inhibition of PKA-C $\alpha$  with recombinant SMO pCT. **c**, As **a**, but comparing wild-type versus WRR mutant versions of the recombinant

SMO pCT. Inhibition in **a–c** is calculated relative to a control without SMO or PKI $\alpha$ (5–24) peptide (Ctrl). Data in **a–c** are shown as the mean  $\pm$  s.d. of two independent experiments. \*\*\* $P$  < 0.001; \*\*\*\* $P$  < 0.0001, NS, not significant. See Supplementary Table 1 for full statistical analysis.

accumulate in cilia but traps it in an inactive conformation<sup>53–55</sup>. We conclude the SMO colocalization with endogenous PKA-C in NIH3T3 cilia is highly specific, as it only occurs when SMO is in an active state.

We next assessed the impact of the SMO PKI motif on PKA-C activity in cells using a model PKA-C substrate, the cyclic AMP response element binding protein (CREB) transcription factor<sup>56</sup> and a CREB transcriptional reporter assay. This experimental model entails overexpression of PKA-C at levels exceeding those of endogenous PKA-R, thereby minimizing potentially confounding contributions from heterotrimeric G protein- and cAMP-containing cascades<sup>29</sup>. Under these conditions, wild-type SMO674 blocked PKA-C-mediated CREB reporter activation while SMO674 harboring the WRR mutation failed to do so (Fig. 6a). We observed similar effects with serine substitution of the P site alanine (A635S, Fig. 6a and Extended Data Fig. 6a), which converts pseudosubstrates to substrates and thereby promotes their dissociation from the PKA-C active site<sup>38,57</sup>.

To capture the entire process of Hh signal transduction from the cell surface to the nucleus, we used mouse embryonic fibroblasts

(MEFs) and a GLI transcriptional reporter assay<sup>11,58,59</sup>. This model strictly requires SMO, PKA-C, GLI and an intact cilium<sup>58,60,61</sup>. In *Smo*<sup>−/−</sup> MEFs, transfection of wild-type SMO enabled strong GLI transcriptional responses to Hh ligands, whereas the WRR and A635S mutants were almost completely devoid of activity (Fig. 6b).

Mutations in the SMO PKI motif specifically affect binding to and inhibition of PKA-C, based on the following control studies. First, the expression levels and electrophoretic mobilities of these mutants were similar to wild-type controls, and the mutants localized correctly to primary cilia (Extended Data Figs. 6a,b and 8). In addition, the SMO mutations only minimally affected BRET with nanobody 2 (NbSmo2, Fig. 4a), which selectively binds the active state of SMO via the cytoplasmic face of its seven-transmembrane (7TM) domain<sup>29</sup>. Finally, the mutants underwent normal SMO activity-dependent phosphorylation by GRK2/3 kinases<sup>29,62</sup> (Extended Data Fig. 8d). These data rule out possible nonspecific effects of the mutations on SMO expression, trafficking, conformational activation or ability to serve as a GRK2/3 substrate.

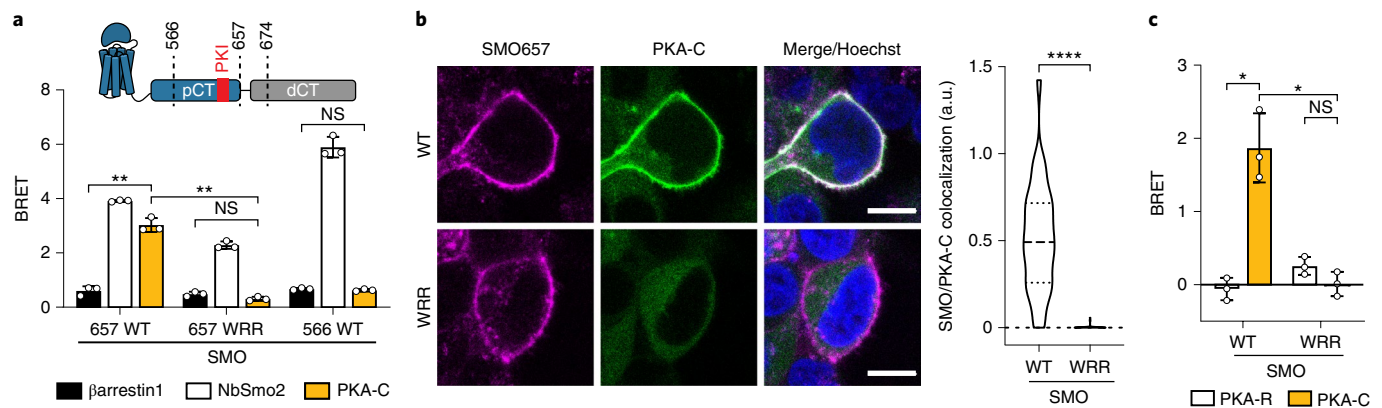


**Fig. 4 | The SMO PKI motifs required for Hh signal transduction.** **a**, Top, schematic diagram of truncated SMO expression constructs. Bottom, BRET analysis of SMO-PKA-C interactions in HEK293 cells expressing nanoluc-tagged wild-type SMO657 (SMO657 WT) or SMO657 harboring the WRR mutation (SMO657 WRR), along with YFP-tagged PKA-C $\alpha$ . SMO566 (which lacks the C-tail) serves as a negative control donor. YFP-tagged  $\beta$ arrestin1 (which exhibits minimal binding to SMO) and NbSmo2 (which binds the intracellular surface of the SMO 7TM domain) serve as negative and positive control acceptors, respectively<sup>29</sup>. Data represent mean  $\pm$  s.d.,  $n = 3$  biologically independent samples. **b**, Left, confocal images of live HEK293 cells coexpressing GFP-tagged PKA-C $\alpha$  with FLAG-tagged wild-type or mutant SMO657. Cells were treated with

SMO agonist (SAG21k). Scale bar, 10  $\mu$ m. Right, quantification of SMO-PKA-C colocalization with the median represented by a dashed line and the upper and lower quartiles indicated by dotted lines ( $n = 34$  or 48 cells for 'WT' or 'WRR', respectively, examined over two independent experiments). **c**, BRET analysis of SMO-PKA-C interactions in IMCD3 cells expressing nanoluc-tagged wild-type or mutant SMO, along with low levels of PKA-C $\alpha$ -YFP. PKA-R $\alpha$ -YFP serves as a negative control. Under these conditions, PKA-C $\alpha$ -YFP is expressed at substantially lower levels than PKA-R $\alpha$ -YFP<sup>29</sup>. Data represent mean  $\pm$  s.d.,  $n = 3$  biologically independent samples. \* $P < 0.05$ ; \*\* $P < 0.01$ , \*\*\*\* $P < 0.0001$ , NS, not significant. See Supplementary Table 1 for full statistical analysis.

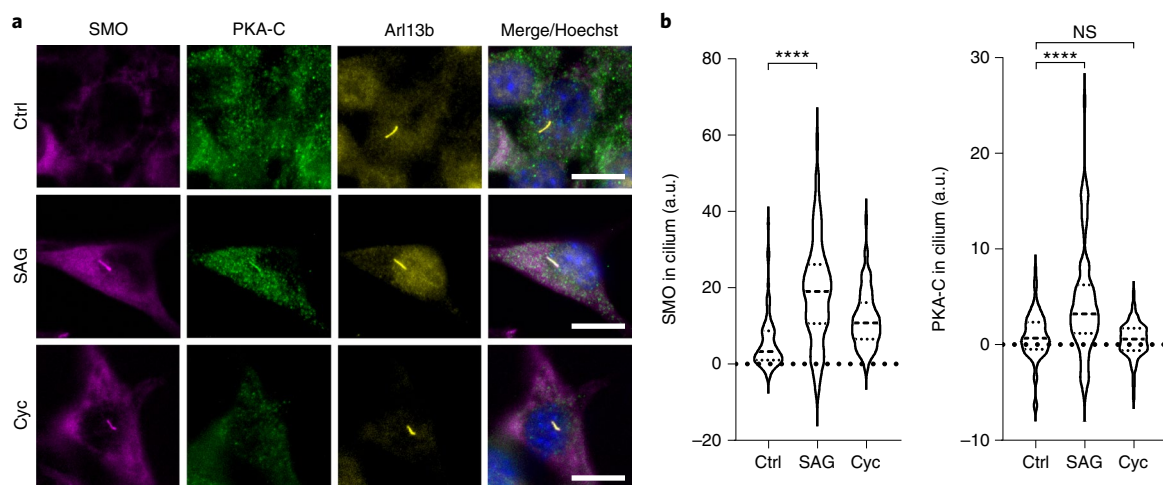


**Fig. 5 | SMO colocalizes with endogenous PKA-C in primary cilia.** **a**, Left, immunofluorescence microscopy images of endogenous PKA-C (green) in NIH3T3 cells stably expressing a V5-TurboID-tagged full-length SMO construct at low levels (Extended Data Fig. 7 and Supplementary Information), and treated with SAG, cyclopamine ('Cyc') or vehicle control ('Ctrl') for 8 h. SMO is marked by a fluorescent streptavidin conjugate (magenta). Cilium is marked by Arl13b

(yellow). Scale bar, 10  $\mu$ m. **b**, Quantification of SMO or PKA-C signal intensity in cilia, with the median represented by a dashed line and the upper and lower quartiles indicated by dotted lines ( $n = 74$ , 81 or 78 cells per condition for 'Ctrl', 'SAG' or 'Cyc', respectively, examined over two independent experiments). \*\*\*\* $P < 0.0001$ , NS, not significant. See Supplementary Table 1 for full statistical analysis.

To examine the role of the SMO PKI motif in Hh signal transduction in vivo, we studied the specification of slow muscle cell types in zebrafish embryos, a widely used model of morphogenetic Hh signal transduction during vertebrate development<sup>29,63,64</sup>. While expression of wild-type SMO restored correct muscle specification to *smo*<sup>-/-</sup> zebrafish, the WRR or A635S mutants did not (Fig. 6c and Supplementary Table 2).

Taken together, our studies demonstrate a requirement for PKA-C pseudosubstrate interactions in SMO inhibition of PKA-C, and activation of GLI, during Hh signal transduction in both cultured cells and organisms.

**An avidity-based mechanism for SMO inhibition of PKA-C**  
PKA-C interactions with the SMO PKI motif, while essential for Hh signal transduction (Fig. 6), appear weaker ( $K_D = 823$ –911 nM for SMO PKI peptides, Fig. 1b and Extended Data Fig. 2a) than those with a canonical PKA-C pseudosubstrate ( $K_D = 1.1$  nM for PKI $\alpha$ (5–24) peptide<sup>46</sup>). SMO-PKA-C interactions, however, are also influenced by sequences outside the PKI motif, indicating that they are more favorable in vivo than the in vitro measurements suggest. Two lines of evidence support this proposal. First, SMO mutations known to reduce PKA-C interactions in vivo, including deletion of a predicted amphipathic helix spanning residues 570–581 or alanine substitution of GRK2/3

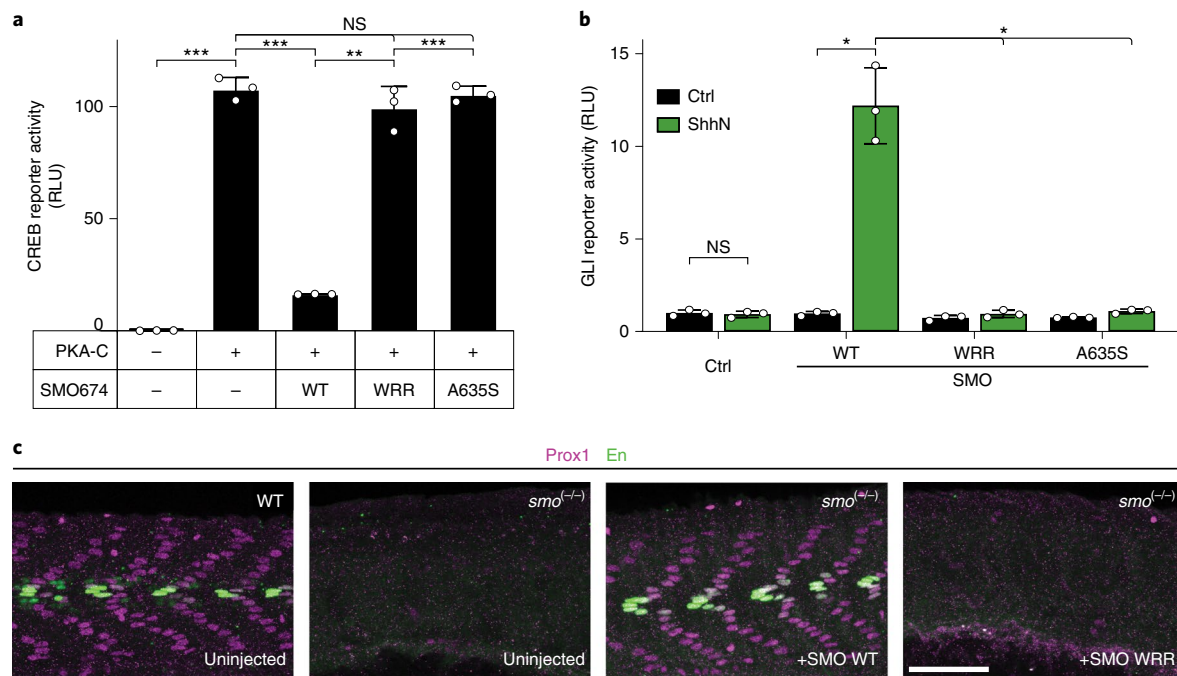


**Fig. 6 | The SMO PKI motif is required for Hh signal transduction.**

**a**, CREB transcriptional reporter assay, reflecting PKA-C mediated substrate phosphorylation, in HEK293 cells transfected with PKA-C $\alpha$  and the indicated SMO674 constructs. Data represent the mean  $\pm$  s.d.,  $n = 3$  biologically independent samples. **b**, GLI transcriptional reporter assay in *Smo*<sup>-/-</sup> MEFs transfected with a GFP negative control (Ctrl), or the indicated wild-type (WT) or mutant SMO constructs. Cells were treated with conditioned medium containing

the N-terminal signaling domain of ShhN (green), or control, non-ShhN-containing conditioned medium (Ctrl, black). Data represent the mean  $\pm$  s.d.,  $n = 3$  biologically independent samples. **c**, Wild-type or *smo*<sup>-/-</sup> zebrafish injected with the indicated mRNA constructs were stained for Prox1 (magenta) or Engrailed (En, green) to mark muscle fiber nuclei.  $n = 12$  (uninjected),  $n = 41$  (SMO WT) and  $n = 47$  (SMO WRR). \* $P < 0.05$ ; \*\* $P < 0.01$ ; \*\*\* $P < 0.001$ ; NS, not significant. See Supplementary Table 1 for full statistical analysis of Fig. 6a,b.

phosphorylation sites<sup>29</sup>, map to non-PKI regions of the pCT (summarized in Fig. 7a). Second, SMO pCT interactions with PKA-C are enhanced by the distal SMO C-tail (dCT, residues 658–793)<sup>29</sup>, demonstrating that this region harbors additional PKA-C binding determinants. Accordingly, in HEK293 cells, PKA-C interactions with SMO containing its full-length C-tail are only partially blocked by the WRR mutation (Fig. 7b), in contrast to the near-complete loss of interaction with SMO lacking the dCT (Fig. 4a),

In light of the above findings, we searched for additional PKA-C binding sequences in the SMO C-tail using a tiled peptide microarray. While this approach is not ideal for detecting binding interactions involving extensive secondary structure, it is well-suited to uncover short linear PKA-C binding motifs within protein domains predicted to be largely unstructured or disordered<sup>65,66</sup>, such as the SMO C-tail<sup>14,29</sup>. Indeed, our microarray identified several PKA-C-binding sequences in addition to the PKI motif, including one in the dCT with PKI-like attributes (Fig. 7c and Extended Data Fig. 9).

Taken together, our data support an avidity-based mechanism for SMO-PKA-C binding. A set of ancillary interactions cooperate to stabilize the core binding events between the SMO PKI motif and the PKA-C active site. This avidity-based mechanism may provide the essential link between SMO activation and disruption of PKA-C phosphoryl transfer during Hh signal transduction.

## Discussion

SMO inhibition of PKA-C is a central aspect of Hh signal transduction in development and disease. Instead of obeying the existing models for GPCR-PKA signaling, SMO enjoys a private signaling pathway whereby it directly binds PKA-C as a pseudosubstrate. This both restricts access of PKA-C to soluble targets and extinguishes its enzymatic activity. A PKI motif encoded by the SMO cytoplasmic domain is central to this mechanism in two ways. First, the PKI motif sequesters PKA-C away

from GLI by promoting SMO-PKA-C interactions, which recruits PKA-C to the ciliary membrane. Second, the PKI motif occludes the PKA-C active site, interrupting catalysis. By using this two-pronged strategy, SMO can efficiently block PKA-C-mediated phosphorylation, activate GLI and promote transcription of Hh pathway target genes.

Based on our findings, we propose a revised model for Hh signal transduction downstream of SMO (Fig. 7d). In the pathway 'off' state, SMO is in an inactive conformation<sup>11,53,59,67</sup>. As a result, SMO cannot be phosphorylated efficiently by GRK2/3 (refs. 29,62), and exists at low levels in the ciliary membrane<sup>54,68,69</sup>. We expect interactions between PKA-C and the SMO PKI motif to be unfavorable under these conditions due to their distinct subcellular localizations and relatively weak affinity. In the pathway 'on' state, Hh-mediated inactivation of PTCH1 enables SMO to bind its endogenous sterol ligands and adopt an active conformation<sup>11–13,59</sup>; alternatively, oncogenic *PTCH1* loss-of-function mutations or *SMO* gain-of-function mutations (such as SMO<sup>M2</sup>) constitutively activate SMO by stabilizing the active conformation of the SMO 7M domain<sup>12,67,70,71</sup>. Consequently, active SMO is recognized by GRK2/3, undergoes phosphorylation of its pCT and accumulates in the cilium, bringing SMO in close proximity to ciliary PKA-C. This allows SMO to bind PKA-C via its PKI motif, which both sequesters PKA-C at the ciliary membrane<sup>29</sup> and blocks PKA-C-mediated catalysis.

Along with the PKI motif, our study identified additional PKA-C-binding sequences in the SMO pCT and dCT (Fig. 7); whereas such sequences cannot support Hh signal transduction in the absence of an intact SMO PKI motif (Fig. 6b,c), they may nevertheless contribute to pathway activation in a more peripheral way, such as by stabilizing the interaction between the PKI motif and the kinase active site. We expect that binding of the SMO PKI motif to PKA-C is also enhanced by the membrane itself, which restricts diffusion of proteins to two dimensions and can thereby dramatically increase effective concentrations relative to soluble compartments<sup>72</sup>. Additionally, SMO activation

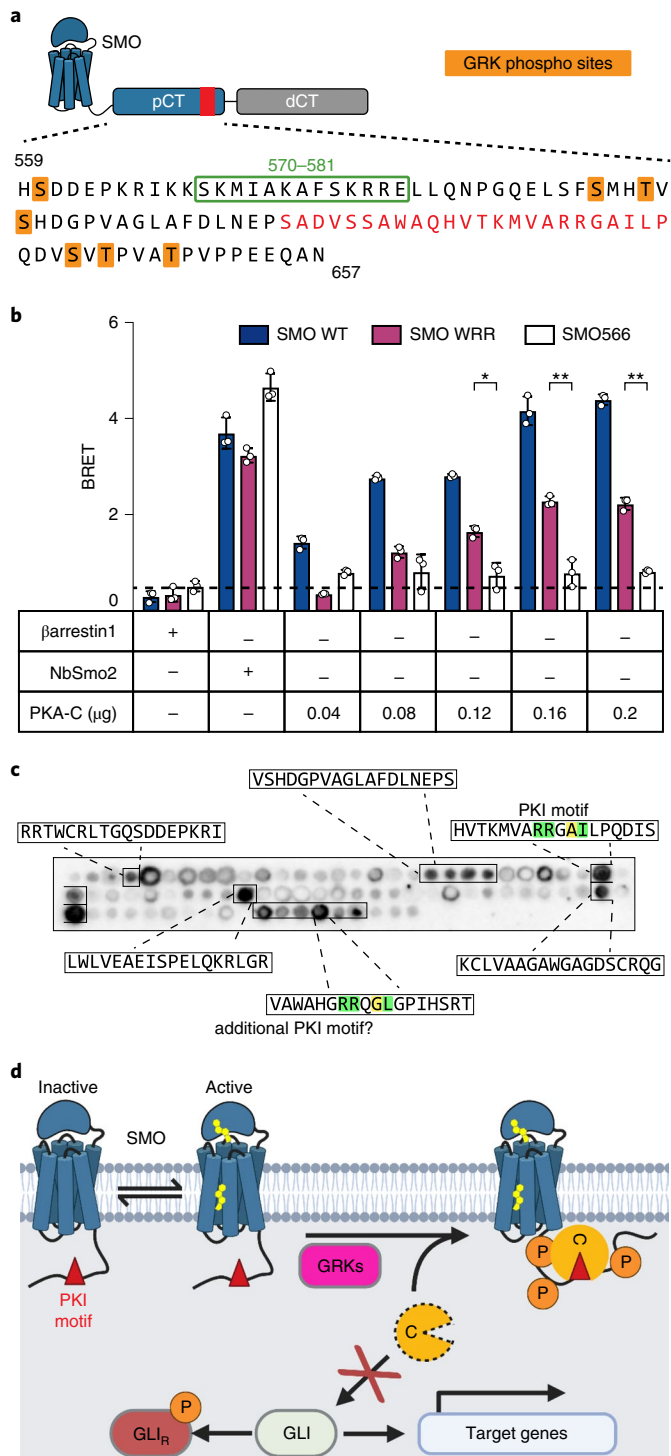


**Fig. 7 | An avidity-based mechanism for SMO inhibition of PKA-C.** **a**, Annotated sequence of the mouse SMO pCT. PKI motif is indicated in red, along with GRK2/3 phosphorylation sites (orange) and residues 570–581 (green box), previously shown to influence SMO–PKA-C interactions and Hh signal transduction<sup>29,54</sup>. **b**, BRET analysis of SMO–PKA-C interactions in HEK293 cells transfected with full-length wild-type SMO (WT, navy) WRR mutant (purple) or C-terminally truncated (SMO566, white) versions of SMO as donor, and the indicated DNA amounts of PKA-C $\alpha$  as acceptor. A nonspecific signal is indicated by the negative control BRET acceptor  $\beta$ arrestin1 (dashed line). Data represent the mean  $\pm$  s.d.,  $n = 3$  biologically independent samples. \* $P < 0.05$ ; \*\* $P < 0.01$ . See Supplementary Table 1 for full statistical analysis. **c**, Representative image of a tiled array of 18mer peptides covering the complete C-tail of human SMO, probed with PKA-C $\alpha$  as in Fig. 1c. Peptides that bind are boxed and their sequences indicated. **d**, Proposed model for Hh signal transduction, as described in the Discussion.

could conceivably decrease ciliary cAMP via coupling to inhibitory ( $G\alpha_{i/o/z}$ ) G protein cascades<sup>59,73,74</sup> or by triggering the ciliary exit of GPR161, a constitutively active GPCR that couples to stimulatory ( $G\alpha_s$ ) G proteins<sup>50,52,75</sup>. These processes, while not absolutely required for Hh signal transduction<sup>75–80</sup>, may reduce levels of free (non-PKA-R-bound) PKA-C in cilia<sup>81</sup>, and thereby aid the SMO PKI motif in binding and inhibiting the ciliary pool of PKA-C. Thus, activation of SMO prevents PKA-C substrate phosphorylation via a host of auxiliary interactions and regulatory influences that assist the essential pseudosubstrate action of the SMO PKI motif.

Our study helps explain a crucial but enigmatic aspect of Hh signal transduction, namely how PKA-C is inhibited, and GLI is activated only when the Hh pathway is in an ‘on’ state. Indeed, our findings are consistent with several previous observations, such as that inactivation of GRK2/3 decreases SMO–PKA-C interactions<sup>29</sup>, blocks SMO–PKA-C colocalization<sup>29</sup> and abolishes Hh signal transduction<sup>64,82,83</sup>. Based on our model, these effects can be explained by GRK2/3 inhibition weakening the SMO–PKA-C interaction below a critical threshold such that the PKI motif cannot efficiently engage the enzyme’s active site. Furthermore, our findings indicate that SMO–PKA-C interactions are appropriately tuned: if the SMO PKI motif were to bind PKA-C with high affinity, the Hh pathway could misfire as PKA-C would be inhibited (and GLI dephosphorylated) even when SMO is inactive, similar to organismal phenotypes observed on loss of PKA-C function<sup>60,84–86</sup>. This proposal is consistent with the relatively modest effects of the SMO pseudosubstrate peptide on the PKA-C amide fingerprint in our NMR studies. Unlike PKI, which functions as a constitutive PKA-C inhibitor, only the active state of SMO is expected to efficiently bind and inhibit PKA-C under physiological conditions. Thus, short peptides containing only the minimal SMO pseudosubstrate sequence but missing the key structural determinants that specify the SMO active state (such as the 7TM domain and GRK2/3 phosphorylation sites) have only a limited capacity to bias PKA-C toward an inactive conformation. Conversely, reducing the affinity of PKA-C for the SMO PKI motif, as occurs with the SMO WRR or A635S mutations, prevents the SMO active state from inhibiting PKA-C and thereby hinders GLI transcription. A similar effect on Hh signaling occurs when PKA-C is ectopically activated<sup>84–86</sup>; although the PKA-C binding site on SMO remains intact under these conditions, the pool of active PKA-C is expanded beyond the capacity for SMO-mediated sequestration and inhibition. Future structural studies of full-length SMO–PKA-C complexes will provide a more detailed mechanistic understanding of how the SMO pCT engages PKA-C, and may also reveal precisely how GRK2/3 facilitates these interactions.

Our model predicts that SMO and PKA-C will interact in cilia under physiological conditions, but only when SMO is in an active conformation. In support of this prediction, we found that endogenous PKA-C colocalizes in NIH3T3 cilia with agonist- but not inverse agonist-bound SMO. These studies focused on endogenous PKA-C subunits, thereby minimizing potential artifactual effects of PKA-C overexpression on endogenous PKA regulatory complexes (Supplementary Information). Our model is consistent with a recent report that stimulation of the Hh pathway decreased PKA-C kinase activity in cilia, as measured by a live-cell fluorescent PKA-C activity reporter<sup>79</sup>. While the authors interpreted their result in terms of potential cAMP-dependent processes downstream of SMO, an alternative and nonmutually exclusive explanation is that SMO directly inhibits PKA-C enzymatic activity via the pseudosubstrate mechanism described here. Going forward, an important goal is to determine the relative stoichiometry of SMO and free (that is, non-PKA-R-bound) PKA-C in cilia (Supplementary Information), as well as these proteins’ activity states within the various ciliary subcompartments where each biochemical step of the pathway occurs. This remains extremely challenging at present given the relatively limited signal-to-noise and spatial resolution of currently available tools. However, new advances in ciliary proteomics and live-cilium biosensors may enable such studies in the future.

The mechanism described above represents a noncanonical mode of GPCR-kinase communication. It is, however, similar to a strategy used by another critical developmental and cancer pathway: the Wnt cascade<sup>87–90</sup> (Extended Data Fig. 10). During the initial steps of Wnt signal transduction at the plasma membrane, the cytoplasmic tail of low-density lipoprotein receptor-related proteins 5/6 (LRP5/6) serves as a pseudosubstrate inhibitor of GSK-3 $\beta$  kinases. This blocks phosphorylation and degradation of the transcriptional coactivator  $\beta$ -catenin<sup>91–94</sup>. Moreover, the LRP5/6 tail binds GSK-3 $\beta$  with low affinity, but Wnt pathway activation enhances this interaction through phosphorylation of the LRP5/6 tail as well as recruitment of GSK-3 $\beta$ -containing protein complexes to the plasma membrane<sup>91–93</sup>. Thus, in both the Hh and Wnt cascades, a phosphorylated receptor tail sequesters and competitively inhibits a kinase via an avidity-based mechanism. It was unexpected that these two pathways, which use distinct molecular components and rely on disparate subcellular environments (cilium versus plasma membrane)<sup>21,95</sup>, nevertheless share a common mechanism for intracellular signal transduction. Why such a mechanism evolved to carry out central steps in these pathways is unclear. One possibility is that it serves to spatially restrict the kinase-inhibiting effects of upstream receptors and thereby avoid pleiotropic effects of inhibiting these kinases globally. This may help to ensure signaling specificity and reduce untoward crosstalk with other pathways<sup>88,91,94</sup>. It is also possible that such a mechanism is particularly well-suited to the embryogenesis- and homeostasis-related functions of Hh and Wnt signaling. In any event, the use of a similar strategy during Hh and Wnt signal transduction hints at a more general applicability to a range of transmembrane receptors and kinases. Given the ubiquity of these proteins in metazoan physiology and disease<sup>22,23,33</sup> and their prevalence as therapeutic targets<sup>96,97</sup>, this mechanism represents an exciting area for future study.

## Online content

Any methods, additional references, Nature Research reporting summaries, source data, extended data, supplementary information, acknowledgements, peer review information; details of author contributions and competing interests; and statements of data and code availability are available at <https://doi.org/10.1038/s41594-022-00838-z>.

## References

- Briscoe, J. & Therond, P. P. The mechanisms of Hedgehog signalling and its roles in development and disease. *Nat. Rev. Mol. Cell Biol.* **14**, 416–429 (2013).
- Ingham, P. W. & McMahon, A. P. Hedgehog signaling in animal development: paradigms and principles. *Genes Dev.* **15**, 3059–3087 (2001).
- Ingham, P. W., Nakano, Y. & Seger, C. Mechanisms and functions of Hedgehog signalling across the metazoa. *Nat. Rev. Genet.* **12**, 393–406 (2011).
- Kong, J. H., Siebold, C. & Rohatgi, R. Biochemical mechanisms of vertebrate hedgehog signaling. *Development* **146**, dev166892 (2019).
- Muenke, M. & Beachy, P. A. Genetics of ventral forebrain development and holoprosencephaly. *Curr. Opin. Genet. Dev.* **10**, 262–269 (2000).
- Digilio, M. C. et al. Atrioventricular canal defect and genetic syndromes: the unifying role of Sonic Hedgehog. *Clin. Genet.* **95**, 268–276 (2019).
- Anderson, E., Peluso, S., Lettice, L. A. & Hill, R. E. Human limb abnormalities caused by disruption of Hedgehog signaling. *Trends Genet.* **28**, 364–373 (2012).
- Pak, E. & Segal, R. A. Hedgehog signal transduction: key players, oncogenic drivers, and cancer therapy. *Dev. Cell* **38**, 333–344 (2016).
- Wu, F., Zhang, Y., Sun, B., McMahon, A. P. & Wang, Y. Hedgehog signaling: from basic biology to cancer therapy. *Cell Chem. Biol.* **24**, 252–280 (2017).
- Hui, C. C. & Angers, S. Gli proteins in development and disease. *Annu. Rev. Cell Dev. Biol.* **27**, 513–537 (2011).
- Deshpande, I. et al. Smoothened stimulation by membrane sterols drives Hedgehog pathway activity. *Nature* **571**, 284–288 (2019).
- Huang, P. et al. Structural basis of Smoothened activation in Hedgehog signaling. *Cell* **174**, 312–324 (2018).
- Byrne, E. F. X. et al. Structural basis of Smoothened regulation by its extracellular domains. *Nature* **535**, 517–522 (2016).
- Qi, X., Friedberg, L., De Bose-Boyd, R., Long, T. & Li, X. Sterols in an intramolecular channel of Smoothened mediate Hedgehog signaling. *Nat. Chem. Biol.* **16**, 1368–1375 (2020).
- Wang, B., Fallon, J. F. & Beachy, P. A. Hedgehog-regulated processing of GLI3 produces an anterior/posterior repressor gradient in the developing vertebrate limb. *Cell* **100**, 423–434 (2000).
- Humke, E. W., Dorn, K. V., Milenkovic, L., Scott, M. P. & Rohatgi, R. The output of Hedgehog signaling is controlled by the dynamic association between Suppressor of Fused and the GLI proteins. *Genes Dev.* **24**, 670–682 (2010).
- Niewiadomski, P. et al. GLI protein activity is controlled by multisite phosphorylation in vertebrate Hedgehog signaling. *Cell Rep.* **6**, 168–181 (2014).
- Li, J. et al. PKA-mediated GLI2 and GLI3 phosphorylation is inhibited by Hedgehog signaling in cilia and reduced in Talpid3 mutant. *Dev. Biol.* **429**, 147–157 (2017).
- Nachury, M. V. & Mick, D. U. Establishing and regulating the composition of cilia for signal transduction. *Nat. Rev. Mol. Cell Biol.* **20**, 389–405 (2019).
- Reiter, J. F. & Leroux, M. R. Genes and molecular pathways underpinning ciliopathies. *Nat. Rev. Mol. Cell Biol.* **18**, 533–547 (2017).
- Gigante, E. D. & Casparly, T. Signaling in the primary cilium through the lens of the Hedgehog pathway. *Wiley Interdiscip. Rev. Dev. Biol.* **9**, e377 (2020).
- Lefkowitz, R. J. The superfamily of heptahelical receptors. *Nat. Cell Biol.* **2**, E133–E136 (2000).
- Pierce, K. L., Premont, R. T. & Lefkowitz, R. J. Seven-transmembrane receptors. *Nat. Rev. Mol. Cell Biol.* **3**, 639–650 (2002).
- Walker-Gray, R., Stengel, F. & Gold, M. G. Mechanisms for restraining cAMP-dependent protein kinase revealed by subunit quantitation and cross-linking approaches. *Proc. Natl Acad. Sci. USA* **114**, 10414–10419 (2017).
- Johnson, D. A., Leathers, V. L., Martinez, A. M., Walsh, D. A. & Fletcher, W. H. Fluorescence resonance energy transfer within a heterochromatic cAMP-dependent protein kinase holoenzyme under equilibrium conditions: new insights into the conformational changes that result in cAMP-dependent activation. *Biochemistry* **32**, 6402–6410 (1993).
- Yang, S., Fletcher, W. H. & Johnson, D. A. Regulation of cAMP-dependent protein kinase: enzyme activation without dissociation. *Biochemistry* **34**, 6267–6271 (1995).
- Kopperud, R. et al. Formation of inactive cAMP-saturated holoenzyme of cAMP-dependent protein kinase under physiological conditions. *J. Biol. Chem.* **277**, 13443–13448 (2002).
- Smith, F. D. et al. Local protein kinase A action proceeds through intact holoenzymes. *Science* **356**, 1288–1293 (2017).
- Arveseth, C. D. et al. Smoothened transduces hedgehog signals via activity-dependent sequestration of PKA catalytic subunits. *PLoS Biol.* **19**, e3001191 (2021).

30. Taylor, S. S., Ilouz, R., Zhang, P. & Kornev, A. P. Assembly of allosteric macromolecular switches: lessons from PKA. *Nat. Rev. Mol. Cell Biol.* **13**, 646–658 (2012).
31. Dalton, G. D. & Dewey, W. L. Protein kinase inhibitor peptide (PKI): a family of endogenous neuropeptides that modulate neuronal cAMP-dependent protein kinase function. *Neuropeptides* **40**, 23–34 (2006).
32. Soberg, K. & Skalhegg, B. S. The molecular basis for specificity at the level of the protein kinase catalytic subunit. *Front Endocrinol. (Lausanne)* **9**, 538 (2018).
33. Taylor, S. S., Zhang, P., Steichen, J. M., Keshwani, M. M. & Kornev, A. P. PKA: lessons learned after twenty years. *Biochim. Biophys. Acta* **1834**, 1271–1278 (2013).
34. Kemp, B. E. & Pearson, R. B. Protein kinase recognition sequence motifs. *Trends Biochem. Sci.* **15**, 342–346 (1990).
35. Scott, J. D., Fischer, E. H., Demaille, J. G. & Krebs, E. G. Identification of an inhibitory region of the heat-stable protein inhibitor of the cAMP-dependent protein kinase. *Proc. Natl Acad. Sci. USA* **82**, 4379–4383 (1985).
36. Cheng, H. C., van Patten, S. M., Smith, A. J. & Walsh, D. A. An active twenty-amino-acid-residue peptide derived from the inhibitor protein of the cyclic AMP-dependent protein kinase. *Biochem. J.* **231**, 655–661 (1985).
37. Corbin, J. D. et al. Studies on the properties and mode of action of the purified regulatory subunit of bovine heart adenosine 3':5'-monophosphate-dependent protein kinase. *J. Biol. Chem.* **253**, 3997–4003 (1978).
38. Scott, J. D., Glaccum, M. B., Fischer, E. H. & Krebs, E. G. Primary-structure requirements for inhibition by the heat-stable inhibitor of the cAMP-dependent protein kinase. *Proc. Natl Acad. Sci. USA* **83**, 1613–1616 (1986).
39. Glass, D. B., Cheng, H. C., Mende-Mueller, L., Reed, J. & Walsh, D. A. Primary structural determinants essential for potent inhibition of cAMP-dependent protein kinase by inhibitory peptides corresponding to the active portion of the heat-stable inhibitor protein. *J. Biol. Chem.* **264**, 8802–8810 (1989).
40. Knighton, D. R. et al. Structure of a peptide inhibitor bound to the catalytic subunit of cyclic adenosine monophosphate-dependent protein kinase. *Science* **253**, 414–420 (1991).
41. Knighton, D. R. et al. Crystal structure of the catalytic subunit of cyclic adenosine monophosphate-dependent protein kinase. *Science* **253**, 407–414 (1991).
42. Johnson, D. A., Akamine, P., Radzio-Andzelm, E., Madhusudan, M. & Taylor, S. S. Dynamics of cAMP-dependent protein kinase. *Chem. Rev.* **101**, 2243–2270 (2001).
43. Olivieri, C. et al. Multi-state recognition pathway of the intrinsically disordered protein kinase inhibitor by protein kinase A. *eLife* **9**, e55607 (2020).
44. Kim, J. et al. The role of ciliary trafficking in Hedgehog receptor signaling. *Sci. Signal* **8**, ra55 (2015).
45. Whitehouse, S. & Walsh, D. A. Mg X ATP2-dependent interaction of the inhibitor protein of the cAMP-dependent protein kinase with the catalytic subunit. *J. Biol. Chem.* **258**, 3682–3692 (1983).
46. Knape, M. J. et al. Divalent metal ions control activity and inhibition of protein kinases. *Metallomics* **9**, 1576–1584 (2017).
47. Cook, P. F. et al. Adenosine cyclic 3',5'-monophosphate dependent protein kinase: kinetic mechanism for the bovine skeletal muscle catalytic subunit. *Biochemistry* **21**, 5794–5799 (1982).
48. Marullo, S. & Bouvier, M. Resonance energy transfer approaches in molecular pharmacology and beyond. *Trends Pharmacol. Sci.* **28**, 362–365 (2007).
49. Machleidt, T. et al. NanoBRET—a novel BRET platform for the analysis of protein-protein interactions. *ACS Chem. Biol.* **10**, 1797–1804 (2015).
50. Mick, D. U. et al. Proteomics of primary cilia by proximity labeling. *Dev. Cell* **35**, 497–512 (2015).
51. Desai, P. B., Stuck, M. W., Lv, B. & Pazour, G. J. Ubiquitin links Smoothed to intraflagellar transport to regulate Hedgehog signaling. *J. Cell Biol.* **219**, e201912104 (2020).
52. Pal, K. et al. Smoothed determines beta-arrestin-mediated removal of the G protein-coupled receptor Gpr161 from the primary cilium. *J. Cell Biol.* **212**, 861–875 (2016).
53. Rohatgi, R., Milenkovic, L., Corcoran, R. B. & Scott, M. P. Hedgehog signal transduction by Smoothed: pharmacologic evidence for a 2-step activation process. *Proc. Natl Acad. Sci. USA* **106**, 3196–3201 (2009).
54. Kim, J., Kato, M. & Beachy, P. A. Gli2 trafficking links Hedgehog-dependent activation of Smoothed in the primary cilium to transcriptional activation in the nucleus. *Proc. Natl Acad. Sci. USA* **106**, 21666–21671 (2009).
55. Wilson, C. W., Chen, M. H. & Chuang, P. T. Smoothed adopts multiple active and inactive conformations capable of trafficking to the primary cilium. *PLoS ONE* **4**, e5182 (2009).
56. Shaywitz, A. J. & Greenberg, M. E. CREB: a stimulus-induced transcription factor activated by a diverse array of extracellular signals. *Annu. Rev. Biochem.* **68**, 821–861 (1999).
57. Knape, M. J. et al. Divalent Metal Ions Mg<sup>2+</sup> and Ca<sup>2+</sup> have distinct effects on protein kinase A activity and regulation. *ACS Chem. Biol.* **10**, 2303–2315 (2015).
58. Varjosalo, M., Li, S. P. & Taipale, J. Divergence of hedgehog signal transduction mechanism between *Drosophila* and mammals. *Dev. Cell* **10**, 177–186 (2006).
59. Myers, B. R., Neahring, L., Zhang, Y., Roberts, K. J. & Beachy, P. A. Rapid, direct activity assays for Smoothed reveal Hedgehog pathway regulation by membrane cholesterol and extracellular sodium. *Proc. Natl Acad. Sci. USA* **114**, E11141–E11150 (2017).
60. Tuson, M., He, M. & Anderson, K. V. Protein kinase A acts at the basal body of the primary cilium to prevent Gli2 activation and ventralization of the mouse neural tube. *Development* **138**, 4921–4930 (2011).
61. Lipinski, R. J., Bijlsma, M. F., Gipp, J. J., Podhaizer, D. J. & Bushman, W. Establishment and characterization of immortalized Gli-null mouse embryonic fibroblast cell lines. *BMC Cell Biol.* **9**, 49 (2008).
62. Chen, W. et al. Activity-dependent internalization of Smoothed mediated by beta-arrestin 2 and GRK2. *Science* **306**, 2257–2260 (2004).
63. Wolff, C., Roy, S. & Ingham, P. W. Multiple muscle cell identities induced by distinct levels and timing of hedgehog activity in the zebrafish embryo. *Curr. Biol.* **13**, 1169–1181 (2003).
64. Zhao, Z. et al. An essential role for Grk2 in Hedgehog signalling downstream of Smoothed. *EMBO Rep.* **17**, 739–752 (2016).
65. Eccles, R. L. et al. Bimodal antagonism of PKA signalling by ARHGAP36. *Nat. Commun.* **7**, 12963 (2016).
66. Sastri, M., Barraclough, D. M., Carmichael, P. T. & Taylor, S. S. A-kinase-interacting protein localizes protein kinase A in the nucleus. *Proc. Natl Acad. Sci. USA* **102**, 349–354 (2005).
67. Taipale, J. et al. Effects of oncogenic mutations in Smoothed and Patched can be reversed by cyclopamine. *Nature* **406**, 1005–1009 (2000).
68. Corbit, K. C. et al. Vertebrate Smoothed functions at the primary cilium. *Nature* **437**, 1018–1021 (2005).
69. Rohatgi, R., Milenkovic, L. & Scott, M. P. Patched1 regulates hedgehog signaling at the primary cilium. *Science* **317**, 372–376 (2007).
70. Xie, J. et al. Activating Smoothed mutations in sporadic basal-cell carcinoma. *Nature* **391**, 90–92 (1998).
71. Sweeney, R. T. et al. Identification of recurrent SMO and BRAF mutations in ameloblastomas. *Nat. Genet.* **46**, 722–725 (2014).

72. Yogurtcu, O. N. & Johnson, M. E. Cytosolic proteins can exploit membrane localization to trigger functional assembly. *PLoS Comput. Biol.* **14**, e1006031 (2018).
73. Riobo, N. A., Saucy, B., Dilizio, C. & Manning, D. R. Activation of heterotrimeric G proteins by Smoothed. *Proc. Natl Acad. Sci. USA* **103**, 12607–12612 (2006).
74. Shen, F., Cheng, L., Douglas, A. E., Riobo, N. A. & Manning, D. R. Smoothed is a fully competent activator of the heterotrimeric G protein G<sub>i</sub>. *Mol. Pharmacol.* **83**, 691–697 (2013).
75. Mukhopadhyay, S. et al. The ciliary G-protein-coupled receptor Gpr161 negatively regulates the Sonic Hedgehog pathway via cAMP signaling. *Cell* **152**, 210–223 (2013).
76. Hwang, S.H. et al. The G protein-coupled receptor Gpr161 regulates forelimb formation, limb patterning and skeletal morphogenesis in a primary cilium-dependent manner. *Development* **145**, dev154054 (2018).
77. Shimada, I. S. et al. Basal suppression of the Sonic Hedgehog pathway by the G-protein-coupled receptor Gpr161 restricts medulloblastoma pathogenesis. *Cell Rep.* **22**, 1169–1184 (2018).
78. Regard, J. B. et al. Activation of Hedgehog signaling by loss of GNAS causes heterotopic ossification. *Nat. Med.* **19**, 1505–1512 (2013).
79. Moore, B. S. et al. Cilia have high cAMP levels that are inhibited by Sonic Hedgehog-regulated calcium dynamics. *Proc. Natl Acad. Sci. USA* **113**, 13069–13074 (2016).
80. Low, W. C. et al. The decoupling of Smoothed from Galphai proteins has little effect on Gli3 protein processing and Hedgehog-regulated chick neural tube patterning. *Dev. Biol.* **321**, 188–196 (2008).
81. Tschaikner, P., Enzler, F., Torres-Quesada, O., Aanstad, P. & Stefan, E. Hedgehog and Gpr161: regulating cAMP signaling in the primary cilium. *Cells* **9**, 118 (2020).
82. Pusapati, G. V. et al. G protein-coupled receptors control the sensitivity of cells to the morphogen Sonic Hedgehog. *Sci. Signal* **11**, eaao5749 (2018).
83. Meloni, A. R. et al. Smoothed signal transduction is promoted by G protein-coupled receptor kinase 2. *Mol. Cell. Biol.* **26**, 7550–7560 (2006).
84. Hammerschmidt, M., Bitgood, M. J. & McMahon, A. P. Protein kinase A is a common negative regulator of Hedgehog signaling in the vertebrate embryo. *Genes Dev.* **10**, 647–658 (1996).
85. Concordet, J. P. et al. Spatial regulation of a zebrafish patched homologue reflects the roles of Sonic Hedgehog and protein kinase A in neural tube and somite patterning. *Development* **122**, 2835–2846 (1996).
86. Barresi, M. J., Stickney, H. L. & Devoto, S. H. The zebrafish slow-muscle-omitted gene product is required for Hedgehog signal transduction and the development of slow muscle identity. *Development* **127**, 2189–2199 (2000).
87. MacDonald, B. T., Tamai, K. & He, X. Wnt/beta-catenin signaling: components, mechanisms, and diseases. *Dev. Cell* **17**, 9–26 (2009).
88. Metcalfe, C. & Bienz, M. Inhibition of GSK3 by Wnt signalling—two contrasting models. *J. Cell Sci.* **124**, 3537–3544 (2011).
89. Nusse, R. & Clevers, H. Wnt/beta-Catenin signaling, disease, and emerging therapeutic modalities. *Cell* **169**, 985–999 (2017).
90. Steinhart, Z. & Angers, S. Wnt signaling in development and tissue homeostasis. *Development* **145**, dev146589 (2018).
91. Piao, S. et al. Direct inhibition of GSK3beta by the phosphorylated cytoplasmic domain of LRP6 in Wnt/beta-catenin signaling. *PLoS ONE* **3**, e4046 (2008).
92. Cselenyi, C. S. et al. LRP6 transduces a canonical Wnt signal independently of Axin degradation by inhibiting GSK3's phosphorylation of beta-catenin. *Proc. Natl Acad. Sci. USA* **105**, 8032–8037 (2008).
93. Wu, G., Huang, H., Garcia Abreu, J. & He, X. Inhibition of GSK3 phosphorylation of beta-catenin via phosphorylated PPPSPXS motifs of Wnt coreceptor LRP6. *PLoS ONE* **4**, e4926 (2009).
94. Stamos, J. L., Chu, M. L., Enos, M. D., Shah, N. & Weis, W. I. Structural basis of GSK-3 inhibition by N-terminal phosphorylation and by the Wnt receptor LRP6. *eLife* **3**, e01998 (2014).
95. Ocbina, P. J., Tuson, M. & Anderson, K. V. Primary cilia are not required for normal canonical Wnt signaling in the mouse embryo. *PLoS ONE* **4**, e6839 (2009).
96. Hauser, A. S., Attwood, M. M., Rask-Andersen, M., Schioth, H. B. & Gloriam, D. E. Trends in GPCR drug discovery: new agents, targets and indications. *Nat. Rev. Drug Discov.* **16**, 829–842 (2017).
97. Oprea, T. I. et al. Unexplored therapeutic opportunities in the human genome. *Nat. Rev. Drug Discov.* **17**, 317–332 (2018).
98. Han, P., Sonati, P., Rubin, C. & Michaeli, T. PDE7A1, a cAMP-specific phosphodiesterase, inhibits cAMP-dependent protein kinase by a direct interaction with C. *J. Biol. Chem.* **281**, 15050–15057 (2006).
99. Kim, J. et al. Dysfunctional conformational dynamics of protein kinase A induced by a lethal mutant of phospholamban hinder phosphorylation. *Proc. Natl Acad. Sci. USA* **112**, 3716–3721 (2015).
100. Olivieri, C. et al. Defective internal allosteric network imparts dysfunctional ATP/substrate-binding cooperativity in oncogenic chimera of protein kinase A. *Commun. Biol.* **4**, 321 (2021).

**Publisher's note** Springer Nature remains neutral with regard to jurisdictional claims in published maps and institutional affiliations.

Springer Nature or its licensor holds exclusive rights to this article under a publishing agreement with the author(s) or other rightsholder(s); author self-archiving of the accepted manuscript version of this article is solely governed by the terms of such publishing agreement and applicable law.

© The Author(s), under exclusive licence to Springer Nature America, Inc. 2022

## Methods

### Cell culture and zebrafish husbandry

HEK293FT cells (gift of P. Beachy, Stanford University), IMCD3 Flp-in cells (gift of P. Jackson, Stanford University), Sf9 cells (gift of K.C. Garcia, Stanford University), *Smo*<sup>-/-</sup> MEFs (gift of P. Beachy, Stanford University) and HEK293-Freestyle cells (gift of R. Majeti, Stanford University) were grown as previously described<sup>29</sup>. NIH3T3 Flp-in cells (gift of R. Rohatgi, Stanford University) were grown according to the manufacturer's instructions in DMEM (MT10013CM, Fisher Scientific) with 10%FBS (MT35010CV, Fisher Scientific). Stably transfected HEK293 Flp-in T-rex cells (gift of D. Julius, UCSF) were constructed and maintained as previously described<sup>11</sup>. IMCD3 stable lines coexpressing FLAG-SMO + PKA-C-mNG or FLAG-SMO +  $\beta$ 2ARNb80-mNG were previously described, and the stable line expressing FLAG-SMO(WRR) + PKA-C-mNG was produced as previously described. Zebrafish were maintained as previously described<sup>29</sup>.

### Antibodies, small molecules and other reagents

SMO agonist 21k (SAG21k) was a gift from P. Beachy. Cmpd101 was obtained from Hello Bio. Rabbit antigreen fluorescent protein (GFP) (which also detects YFP) was obtained from ThermoFisher Scientific (A11122). SAG (S7779) and Cyclopamine (S1146) were obtained from Selleckchem. Poly-D-lysine (A003E) and Biotin (B4501-1G) were obtained from Sigma. 20% PFA was obtained from Electron Microscopy Science (15713). Hygromycin B (10687010) and Lipofectamine 2000 reagent (52887) were from Invitrogen. Mouse anti-V5 (R960-25) was obtained from ThermoFisher. Mouse anti-Arl13b was obtained from Antibodies Inc. (75–287, IMCD3 studies) and rabbit anti-Arl13b was obtained from ProteinTech (17711-1-AP, NIH3T3 studies). Mouse anti-Prox1 was obtained from the Monoclonal antibody facility, University of Oregon (4D9), and rabbit anti-engrailed was obtained from AngioBio (11-002P). Purified mouse anti-PKA-C was from BD Biosciences (610980). Rhodamine antirabbit IgG (711025152), Alexa 488 antimouse IgG (715545150), Alexa647 streptavidin (016600084) were obtained from Jackson ImmunoResearch. Alexa647-conjugated M1 FLAG antibody and M1 FLAG affinity resin were prepared in-house. Control or Sonic Hedgehog (ShhN) conditioned medium was prepared from stably transfected HEK293 cells as previously described<sup>29</sup>. Dual-luciferase assay was obtained from Promega. Coelenterazine h was obtained from NanoLight Technology (301–500). Furimazine was obtained from AOBIOUS (AOB36539). For transfection studies, TransIT 2020 and TransIT 293 were obtained from Mirus Bio.

### DNA constructs

For expression and purification of the SMO pCT in *Escherichia coli*, the ShhN gene was excised from ShhN/pHTSHP<sup>59</sup> and replaced with residues 565–657 of mouse SMO (<sup>565</sup>KRIKK...<sup>657</sup>PEEQAN<sup>657</sup>), downstream of the MBP-His<sub>6</sub>-SUMO tags in the vector pHTSHP, or for glutathione S-transferase (GST) constructs in the vector pGexKG. The resulting construct was termed SMO pCT(565–657). GST-PKI construct in pGexKG was previously described<sup>101</sup>. The SMO655-nanoluc, SMO674 and SMO-nanoluc constructs (all in pVLAD6, with N-terminal hemagglutinin signal sequence and FLAG tag) were previously described<sup>29</sup>. Full-length SMO (in pGEN, with C-terminal myc tag) was previously described<sup>102</sup>. Mouse PKA-C $\alpha$ -YFP, PKA-R1 $\alpha$ -YFP and NbSmo2-YFP constructs in pVLAD6 were previously described<sup>29</sup>. Barrestin1-YFP in pCDNA3.1-zeo was previously described<sup>29</sup>. To construct IMCD3 Flp-in stable lines coexpressing FLAG-tagged mutant SMO with mNeonGreen-tagged PKA-C $\alpha$  (using an IRES element), the previously described construct SMO-IRES-PKA-C $\alpha$ mNG/pEF5-FRT (ref. <sup>29</sup>) was modified to introduce the WRR mutation into SMO. To construct stable Flp-in HEK293 cell lines coexpressing wild-type or mutant SMO674 (which includes an N-terminal hemagglutinin signal sequence and FLAG tag) along with GFP-tagged PKA-C $\alpha$ , we cloned a SMO674-IRES-PKA-C $\alpha$ GFP cassette into the pCDNA5-FRT-TO vector. Untagged human and mouse PKA-C $\alpha$

constructs in the vector pRSETb were previously described<sup>101</sup>. TurboID is a gift from A. Ting's laboratory at Stanford. mSmo-V5-TurboID was inserted into the pEF5-FRT expression vector following the vendor's instruction (ThermoFisher no. V602020). Sequences of all oligonucleotides are provided in Supplementary Table 3. All mutant DNA sequences were prepared via PCR-based mutagenesis, cloned into their respective vector backbones via Gibson assembly and verified by Sanger sequencing.

### Peptide synthesis

SMO PKI peptides (standard = SADVSSAWAQHVTKMVARRGAILP; extended = SADVSSAWAQHVTKMVARRGAILPQDVSVTPVATPVPPP) were prepared via standard solid-phase synthesis by either GenScript or Elim Bio, purified via reversed-phase high-performance liquid chromatography to  $\geq 85\%$  purity and the sequence/molecular mass confirmed by mass spectrometry. A WRR mutant version of the extended SMO peptide was synthesized and validated in the same manner. For fluorescence polarization assays, a FAM fluorophore and 3xPEG linker were added to the N terminus of the standard SMO PKI peptide during synthesis. PKI $\alpha$ (5–24) peptide (TTYADFIASGRTGRRNAIHD) was synthesized as described for the SMO PKI peptides by GeneCust.

### Fluorescence polarization assays

Human or mouse PKA-C $\alpha$  subunits were purified as previously described<sup>103</sup>. In addition, the protein obtained from the S200 was further purified via cation exchange chromatography. For this, the S200 peak fractions were pooled and dialyzed overnight into MonoS buffer (20 mM KH<sub>2</sub>PO<sub>4</sub> pH 6.5, 5 mM DTT) before loading onto a MonoS cation exchange column. PKA-C $\alpha$  was eluted with a gradient of 0–300 mM KCl in MonoS buffer. Binding of a SMO peptide containing the PKI motif was investigated by fluorescence polarization. Assay buffer for all fluorescence polarization experiments consisted of 50 mM MOPS pH 7, 35 mM NaCl, 10 mM MgCl<sub>2</sub>, 1 mM DTT and 0.005% Triton X-100 with the addition of 1 mM ATP in the PKA-C titrations. Experiments were performed by adding 50  $\mu$ l of the titration component (PKA-C or ATP) to 150  $\mu$ l of FAM-SMO containing solution. For SMO-PKA-C binding experiments, a twofold dilution series from 16 to 0  $\mu$ M of either mouse or human PKA-C $\alpha$  was added to 40 nM FAM-SMO. To assess the ATP dependence of SMO binding to PKA-C, a titration with varying the ATP concentration from 0 to 1 mM (human PKA-C $\alpha$ ) or 12.8  $\mu$ M (mouse PKA-C $\alpha$ ) was used with keeping PKA-C at 3  $\mu$ M and FAM-SMO at 25 nM. Readings were taken with a Tecan Genios plate reader using black flat bottom 96-well Costar plates. Each experiment was repeated in at least two independent trials with each condition representing triplicate measurements with FAM readings at 485 nm excitation and 535 nm emission.

### Peptide arrays

Peptide arrays were synthesized with a MultiPep Flexible Parallel Peptide Synthesizer (Intavis Bioanalytical Instruments). The blots were probed with mouse or human PKA-C $\alpha$  protein, purified as described above in the section Fluorescence polarization assays. Unless noted otherwise, all steps were carried out at room temperature. The blots were initially soaked with 100% ethanol for 5 min followed by 5 min of washes for five times with water. All subsequent washes were carried out for 5 min for five times with Tween-Tris-buffered saline (TTBS). The membranes were washed with TTBS, blocked with 5% milk in TTBS for 1 h and washed again with TTBS. They were then soaked with TTBS containing 2  $\mu$ g of PKA-C $\alpha$ , 5% milk, 10 mM MgCl<sub>2</sub> and 1 mM ATP overnight at 4 °C. The next day, the blots were washed, blocked with 5% milk in TTBS and washed again before incubation overnight at 4 °C with TTBS containing 5% milk and a primary PKA-C antibody (generated in-house previously). The next day, the blots were washed, then incubated with an horseradish peroxidase-conjugated antirabbit antibody (Prometheus) in 5% milk TTBS for 1 h followed by a final round of washes

with TTBS. The membranes were finally covered with SuperSignal West Pico PLUS Chemiluminescent Substrate for detection of horseradish peroxidase (Thermo Scientific no. 34580) and imaged with a ChemiDoc MP Imaging System from BIO RAD. A representative array image (representative of two separate trials) is shown; we excluded from analysis any spots that were not observed consistently across replicates.

### SPR

Mouse PKA-C $\alpha$  was overexpressed in *E. coli* BL21(DE3) cells after induction with 0.4 mM isopropyl- $\beta$ -D-thiogalactoside (IPTG) for 16 h at room temperature using the expression vector pRSETb-mPKAC $\alpha$  and then purified by affinity chromatography using an IP20-resin as described earlier<sup>104</sup>. GST-PKI, GST-SMO pCT wild-type and WRR mutant were overexpressed in *E. coli* BL21(DE3) for 16 h at room temperature, and the GST-fusion proteins were purified using Protino glutathione agarose 4B according to the manufacturer's instruction (Macherey-Nagel). Protein-rich fractions were pooled followed by a buffer exchange via PD-10 desalting column (Cytiva) against low-salt buffer (20 mM Tris-HCl, pH 8.0, 25 mM NaCl). The protein was further purified by loading onto a 1 ml of ResourceQ anion exchange column (Cytiva) pre-equilibrated in low-salt buffer. Column was washed extensively with low-salt buffer and protein was eluted with a gradient 0 to 100% high-salt buffer (20 mM Tris-HCl, pH 8.0, 500 mM NaCl). Fractions containing the wild-type and WRR mutant GST-SMO pCT were pooled, respectively. SPR interaction studies were performed according to previous studies<sup>57,101</sup>. Briefly, the interaction studies were performed in running buffer (20 mM MOPS, pH 7.0, 150 mM NaCl, 50  $\mu$ M EDTA, 0.005% P20 surfactant) at 25 °C using a Biacore T200 instrument (GE Healthcare). For measurements involving ATP/MgCl<sub>2</sub>, the buffer was supplemented with 1 mM ATP and 10 mM MgCl<sub>2</sub>. Polyclonal anti-GST antibody (Carl Roth, 3998.1) was covalently immobilized to all four flow cells of a CM5 sensorchip (Cytiva) to a level of 8,000 response units (RU) via standard NHS/EDC amine coupling. Each measurement cycle started with the sequential capture of 40–60 RU of GST-PKI and 125–200 RU of free GST, GST-SMO-RLG WT and GST-SMO-RLG WRR mutant on separate flow cell (flow rate 10  $\mu$ l min<sup>-1</sup>). Interaction analysis was then initiated by the injection of increasing concentrations of PKA-C $\alpha$  (5 nM–2.5  $\mu$ M) at a flow rate of 30  $\mu$ l min<sup>-1</sup> for 120 s (association) followed by 120 s dissociation with buffer without PKA-C $\alpha$ . Nonspecific binding was removed by subtracting SPR signals from the flow cell with only GST protein captured and additional buffer blank runs without PKA-C $\alpha$  (double referencing) using Biacore T200 Evaluation Software 3.0 (Cytiva). After each cycle, the sensorchip was regenerated by injecting up to five times with 10 mM glycine, pH 1.9 or 2.2, to remove the GST-fusion proteins from the antibody surfaces until the baseline level was reached. We carried out steady-state analysis with Biacore T200 Evaluation Software v.3.0.

### NMR spectroscopy

Recombinant human PKA-C $\alpha$  (encoded by the *PRKACA* gene, UniProt P17612) was expressed and purified as reported<sup>100,105</sup>. Briefly, transformed *E. coli* BL21 (DE3) pLysS (Agilent) cells were cultured in deuterated (<sup>2</sup>H) M9 minimal medium supplemented with <sup>15</sup>NH<sub>4</sub>Cl. Protein overexpression was initiated by adding 0.4 mM of isopropyl  $\beta$ -D-1-thiogalactopyranoside (IPTG) and carried out for 12 h at 20 °C. The collected cell pellet was then resuspended in 50 mM Tris-HCl pH 8.0, 30 mM KH<sub>2</sub>PO<sub>4</sub>, 200 mM NaCl, 5 mM  $\beta$ -mercaptoethanol, 0.15 mg ml<sup>-1</sup> lysozyme, 200  $\mu$ M ATP, DnaseI and protease inhibitor (Sigma), and passed through a French press (twice). The cell resuspension was then cleared by centrifugation (40,000g for 45 min), and the supernatant was incubated overnight with Ni<sup>2+</sup>-NTA resin (ThermoFisher). His-tagged PKA-C $\alpha$  was eluted using 50 mM Tris-HCl pH 8.0, 30 mM KH<sub>2</sub>PO<sub>4</sub>, 100 mM NaCl, 5 mM  $\beta$ -mercaptoethanol and 1 mM phenylmethylsulfonyl fluoride supplemented with 200 mM of imidazole. The His-tag was removed during an overnight dialysis step performed

in 20 mM KH<sub>2</sub>PO<sub>4</sub> (pH 6.5), 25 mM KCl, 5 mM  $\beta$ -mercaptoethanol and 0.1 mM phenylmethylsulfonyl, using stoichiometric quantities of recombinant tobacco etch protease. Finally, cationic exchange chromatography was performed to separate the three different isoforms of PKA-C $\alpha$ , representing the three different phosphorylation states of the kinase, using a linear gradient of KCl in 20 mM KH<sub>2</sub>PO<sub>4</sub> at a pH of 6.5 (HiTrap HP SP column, GE Healthcare Life Science). All the NMR experiments were performed using PKA-C $\alpha$  isoform II, corresponding to phosphorylation at S10, T197 and S338 residues<sup>106</sup>. The purity of the protein preparation was tested using SDS-PAGE electrophoresis and mass spectrometry analysis (purity >97%).

A portion of the lyophilized extended SMO PKI peptide (above) was resuspended in 20 mM KH<sub>2</sub>PO<sub>4</sub> (pH 6.5), 90 mM KCl, 10 mM MgCl<sub>2</sub>, 10 mM DTT, 1 mM NaN<sub>3</sub>, to a final concentration of 4 mM. The NMR experiments were performed on 100  $\mu$ M uniformly <sup>2</sup>H, <sup>15</sup>N-labeled PKA-C $\alpha$  sample in 20 mM KH<sub>2</sub>PO<sub>4</sub>, 90 mM KCl, 10 mM MgCl<sub>2</sub>, 10 mM DTT, 1 mM NaN<sub>3</sub> at a pH of 6.5 and saturated with 12 mM of a nonhydrolyzable ATP analog (ATP $\gamma$ N). Modified [<sup>1</sup>H-<sup>15</sup>N]-TROSY-HSQC spectra<sup>107</sup> were acquired on a Bruker Avance III spectrometer operating at a proton frequency of 850 MHz and on a 600 MHz Bruker Avance NEO spectrometer, equipped with a TCI cryoprobe, at an acquisition temperature of 300 K. First, a spectrum of ATP $\gamma$ N-saturated PKA-C $\alpha$  complex (PKA-C $\alpha$ -ATP $\gamma$ N) was recorded with 2,048 (proton) and 128 (nitrogen) complex points. Stoichiometric amounts of SMO PKI peptide (hereafter referred to as SMO PKI) were then added to the PKA-C $\alpha$ -ATP $\gamma$ N complex until saturation (1:0, 1:1, 1:2 and 1:4 SMO PKI:PKA-C/ATP $\gamma$ N molar ratio), with a concentration of SMO PKI ranging from 0.1 to 0.4 mM. The same set of experiments was repeated for the PKA-C titrations with the WRR mutant. Briefly, lyophilized SMO PKI WRR mutant was resuspended in the NMR buffer to a final concentration of 5 mM. Stoichiometric amount of this solution was added to the ATP $\gamma$ N-bound PKA-C $\alpha$  (100  $\mu$ M) until saturation, with 1:0, 1:1, 1:2, 1:4 and 1:6 PKA-C $\alpha$ :ATP $\gamma$ N:SMO WRR molar ratios. A [<sup>1</sup>H, <sup>15</sup>N]-TROSY spectrum<sup>107</sup> was recorded after each addition. All the spectra were processed using NMRPipe<sup>108</sup>, and visualized using NMRFAM-SPARKY software<sup>109</sup>. Combined CSPs were calculated using the <sup>1</sup>H and the <sup>15</sup>N chemical shift derived from the PKA-C $\alpha$ -ATP $\gamma$ N complex and the 1:4 SMO PKI:PKA-C-ATP $\gamma$ N complex. The CSPs were calculated using the following equation<sup>110</sup>:

$$\Delta\delta = \delta_{\text{SMO}} - \delta_{\text{ATP}\gamma\text{N}} = \sqrt{(\Delta\delta\text{H})^2 + (0.154 \times \Delta\delta\text{N})^2}$$

The PKI $\alpha$ (5–24) CSPs were originally published earlier<sup>100</sup> and are included here for reference.

For the displacement experiments, stoichiometric quantities of PKI $\alpha$ (5–24) ranging from 0.05 to 0.6 mM total concentration (1:0, 1:0.5, 1:0, 1:1, 1:2, 1:4 and 1:6 PKA-C/ATP $\gamma$ N:PKI $\alpha$  molar ratio) were added to a SMO PKI-bound PKA-C $\alpha$ -ATP $\gamma$ N complex (1:6 PKA-C $\alpha$ :SMO PKI molar ratio). All the experiments were carried out under the same conditions used for the titration of SMO PKI WT.

### Purification of SMO pCT for PKA-C activity assays

MBP-His<sub>8</sub>-SUMO-tagged SMO pCT (SMO pCT(565–657)/pHTSHP) was transformed into BL21 (DE3) *E. coli* and grown to OD<sub>600</sub> of roughly 0.5–1.0 in 1 l of terrific broth (with ampicillin at 37 °C in 2,800 ml baffled Fernbach flasks. IPTG was then added to 0.4 mM and the temperature lowered to 18 °C for 18 h. Cells were collected by centrifugation (5,000g), snap-frozen in liquid nitrogen and stored at –80 °C. Cell pellets were resuspended in 20 ml binding buffer (50 mM Tris pH 8.0, 300 mM NaCl, 10 mM imidazole, protease inhibitors (Pierce)) at 4 °C with stirring. Lysozyme was added at 1 mg ml<sup>-1</sup> as well as benzonase (10,000 $\times$ , Sigma), and samples were lysed by sonication. Lysates were clarified by centrifugation at 40,000g, 30 min, 4 °C. Supernatant was run by gravity over a column of 6 ml NiNTA affinity resin (Qiagen) pre-equilibrated in binding buffer. The column was washed twice with 5 column volumes of wash buffer (50 mM Tris pH 8.0, 300 mM

NaCl, 25 mM imidazole) and eluted with four successive 1 column volumes of elution buffer (50 mM Tris pH 8.0, 300 mM NaCl, 250 mM imidazole). Protein content of fractions was estimated by Quickstart Bradford assay and purity determined by SDS-PAGE. Protein-rich fractions were pooled and cleaved by the addition of 1.4 mg Ulp1 enzyme (prepared in-house) and 1 mM DTT for 1 h at room temperature. After incubation, the samples were dialyzed overnight against dialysis buffer (50 mM HEPES pH 8.0, 150 mM NaCl, 7 mM  $\beta$ -mercaptoethanol). The completed digestion reaction was applied to NiNTA resin, washed twice with 3 column volumes of dialysis buffer and eluted with 3 column volumes of elution buffer. The flow-through and wash fractions were pooled, centrifugated at 20,000g, 5 min, 4 °C to pellet any insoluble material and further purified by loading onto a 1 ml HiTrap HP SP cation exchange column pre-equilibrated in low-salt buffer (50 mM HEPES pH 8.0, 150 mM NaCl). Column was washed extensively with low-salt buffer and protein was eluted with a gradient to high-salt buffer (50 mM HEPES pH 8.0, 1.2 M NaCl). Fractions containing the cleaved SMO pCT were pooled, concentrated and injected onto a Superdex 200 (10/300) gel filtration column equilibrated in-gel filtration buffer (50 mM HEPES pH 7.5, 300 mM NaCl). The peak fractions were collected and analyzed by SDS-PAGE. Fractions containing intact pCT were pooled, snap-frozen in liquid nitrogen and stored at -80 °C. For the experiments in Fig. 3c, wild-type or mutant pCT proteins were purified by NiNTA affinity as described above and used directly in PKA-C activity assays.

### In vitro PKA-C activity assays

For in vitro PKA-C activity assays, recombinant mouse PKA catalytic subunit (C $\alpha$ ) was overexpressed in *E. coli* BL21(DE3) cells after induction with 0.4 mM IPTG for 14 h at room temperature using the expression vector pRSETb/mPKAC $\alpha$  and then purified by affinity chromatography using an IP20-resin as described earlier<sup>104</sup>. PKA catalytic activity was assayed using a coupled spectrophotometric assay as described previously<sup>47</sup>. Briefly, the reaction mixture contained 100 mM MOPS (pH 7), 10 mM MgCl<sub>2</sub>, 100  $\mu$ M ATP, 1 mM phosphoenolpyruvate, 15 U ml<sup>-1</sup> lactate dehydrogenase, 70 U ml<sup>-1</sup> pyruvate kinase, 200 mM reduced nicotinamide adenine dinucleotide, 5 mM  $\beta$ -mercaptoethanol with 15–30 nM C $\alpha$  and 260  $\mu$ M Kemptide (LRRASLG; GeneCust) as a substrate. Formation of PKA-C-SMO complex (concentrations of SMO peptide or recombinant SMO pCT protein are indicated in the figures) was carried out for 3 minutes at room temperature in the assay mixture. The apparent IC<sub>50</sub> for SMO pCT were determined by fitting the concentration-dependent activity to a sigmoid dose-response model. All data were plotted as means of at least two independent experiments measured in duplicate each with standard deviation (s.d.) ( $n = 4$ – $24$  data points per condition).

### MALS

Purified SMO pCT was concentrated to 5 mg ml<sup>-1</sup> and analyzed using multi-angle light scattering coupled with size-exclusion chromatography with a Superdex 75 gel chromatography column (GE Healthcare) equilibrated in-gel filtration buffer (50 mM HEPES pH 7.5, 300 mM NaCl) and with an in-line DAWN MALS detector (Wyatt Technology).

### BRET

BRET in HEK293 or IMCD3 cells was performed as previously described<sup>29</sup>. Briefly, HEK293 or IMCD3 cells were transiently transfected with 1.2  $\mu$ g DNA made up of nanoluc-tagged SMO (0.3  $\mu$ g) along with YFP-tagged  $\beta$ arrestin1 (0.3  $\mu$ g), NbSmo2 (0.9  $\mu$ g), PKA-C $\alpha$  (0.1  $\mu$ g) or PKA-Rl $\alpha$  (0.1  $\mu$ g) plasmids. The amount of DNA was kept constant in each condition by the addition of empty pV1392 plasmid. We used these amounts of plasmid for all experiments with the following two exceptions: (1) Fig. 4b that examined a range of PKA-C $\alpha$  DNA amounts as indicated in the figure legend; (2) Fig. 3d that used 0.3  $\mu$ g of PKA-C $\alpha$ -YFP (corresponding to a 0.33–2.68% increase in the size of the

endogenous PKA-C pool, as determined by quantitative immunoblotting<sup>29</sup>) or PKA-Rl $\alpha$ -YFP (which displays no BRET with SMO even though it expresses at substantially higher levels than PKA-C $\alpha$ -YFP<sup>29</sup>). Cells were replated in poly-D-lysine-coated white opaque 96-well plates, loaded with 5  $\mu$ M coelenterazine h (HEK293) or 10  $\mu$ M furimazine (IMCD3), and analyzed for BRET on a Tecan Spark multimode plate reader. The background signal from cells expressing nanoluc-tagged SMO without BRET acceptor was subtracted from all measurements. For all BRET assays, data represent mean  $\pm$  s.d. from triplicate wells and data are representative of at least two independent experiments.

### Flow cytometry

Cell-surface expression of wild-type and mutant SMO constructs was analyzed via flow cytometry as previously described<sup>29</sup>. Briefly, HEK293-Freestyle cells were infected with BacMam viruses encoding the indicated wild-type or mutant SMO674 constructs. 1–2 days later, live cells were stained with Alexa647-conjugated M1 anti-FLAG antibody (1:1,000, 5 min) and analyzed on a Cytoflex flow cytometer (Beckman Coulter). To determine the percentage of positive cells, a gate was established and the percent of cells falling within that gate was calculated. This was repeated on two independent occasions.

### CREB reporter assays

CREB transcriptional reporter assays were performed as previously described<sup>29</sup>. Briefly, HEK293FT cells were transfected in 24-well plates with a 30:1 mixture of CRE-Firefly reporter (pGL4.29[luc2p/CRE/Hygro]) and constitutively expressing SV40-Renilla plasmids (20% (w/w)), PKA-C $\alpha$  (0.625% (w/w)), along with the indicated wild-type or mutant SMO674 plasmids (24% (w/w)). A GFP expression plasmid was used to bring the total amount of DNA in each well to 250 ng. Two days later, reporter activity was measured via dual-luciferase assay. Reporter activity is expressed as a ratio of Firefly/Renilla (relative luciferase units (RLU)). For all CREB assays, data represent mean  $\pm$  s.d. from triplicate wells and data are representative of at least two independent experiments.

### Coimmunoprecipitation assay

SMO-PKA-C coimmunoprecipitation was performed as previously described<sup>29</sup>, with minor modifications. Briefly, 3 ml HEK293-Freestyle cells were infected with BacMam viruses encoding PKA-C $\alpha$ -YFP the indicated wild-type or mutant SMO674 constructs and solubilized in low-salt solubilization buffer (20 mM HEPES pH 7.5, 150 mM NaCl, 0.1 mM TCEP, 0.5% GDN, 1 mM CaCl<sub>2</sub>·6H<sub>2</sub>O, protease inhibitor tablet) to prepare a whole-cell lysate. A portion of the lysate was reserved for SDS-PAGE analysis, and the remainder was incubated with FLAG affinity resin (10  $\mu$ l of settled resin per condition). After a 1 h of incubation, resin was washed three times in low-salt wash buffer (20 mM HEPES pH 7.5, 150 mM NaCl, 0.1 mM TCEP, 0.05% GDN, 1 mM CaCl<sub>2</sub>·6H<sub>2</sub>O) and protein eluted in 40  $\mu$ l of the same buffer supplemented with 5 mM EDTA and 0.2 mg ml<sup>-1</sup> FLAG peptide. Proteins were separated by SDS-PAGE on a 4–20% Stain-Free TGX gel (BioRad), and total protein in lysate or eluate was visualized via Stain-Free imaging. To detect PKA-C $\alpha$ -YFP, inputs and eluates were transferred to polyvinylidene difluoride membranes and processed for immunoblotting with anti-GFP antibodies (1:5,000) as previously described<sup>29</sup>. In-gel Pro-Q Diamond assay to detect phosphoprotein was performed according to the manufacturer's instructions, as previously described<sup>29</sup>. Presented data are representative of experiments repeated in at least two independent trials.

### HEK293 imaging

Imaging and quantification of SMO-PKA-C colocalization in HEK293 cells were performed as previously described<sup>29</sup>, with minor modifications. Briefly, HEK293 Flp-in T-rex stable cell lines coexpressing GFP-tagged PKA-C $\alpha$  with either wild-type or mutant FLAG-tagged SMO674 were plated onto  $\mu$ -slide eight-well glass chamber slides (ibidi),

and treated overnight with  $1 \mu\text{g ml}^{-1}$  doxycycline (to induce SMO expression) and  $1 \mu\text{M}$  SAG21k (to induce SMO activation). Live cells were subsequently stained for 5 min with an Alexa647-conjugated M1 anti-FLAG antibody (1:2,000) followed by washing in Hank's buffered saline solution, mounting and visualization. Images were collected on a Leica SP8 laser scanning confocal microscope, using a  $\times 40$  water immersion lens. All images were acquired with identical zoom/exposure/gain settings and processed identically in Fiji. SMO-PKA-C colocalization was determined by measuring the background-subtracted PKA-C (green) fluorescence at the membrane ( $\text{GFP}_{\text{membrane}} - \text{GFP}_{\text{cytoplasm}}$ ) and the background-subtracted SMO (red) fluorescence at the membrane ( $\text{Alexa647}_{\text{membrane}} - \text{Alexa647}_{\text{cytoplasm}}$ ), using four independent line-scans across the membrane in Fiji. The background-subtracted green fluorescence divided by the background-subtracted red fluorescence is referred to as 'SMO-PKA-C colocalization' and reported in arbitrary units (a.u.). The imaging was repeated on multiple occasions and all data were pooled together to generate the plots/quantification in the relevant figure panels.

### IMCD3 imaging

Imaging and quantification of SMO ciliary accumulation and SMO-PKA-C colocalization in IMCD3 cells were performed as previously described<sup>29</sup>. Briefly, to assess ciliary accumulation of wild-type or mutant SMO, IMCD3 cells were transiently transfected on coverslips with the indicated myc-tagged wild-type or mutant SMO-pGEN constructs, grown to confluency, fixed and permeabilized. Coverslips were then stained with anti-myc (SMO) and anti-Arl13b (cilia) antibodies, along with 4,6-diamidino-2-phenylindole to mark the nucleus. For quantitative assessment of SMO-PKA-C colocalization in live IMCD3 cilia, Flp-in IMCD3 cell lines coexpressing mNeonGreen-tagged PKA-C $\alpha$  with either wild-type or mutant FLAG-tagged SMO were plated onto  $\mu$ -slide eight-well glass chamber slides (ibidi), grown to confluency and treated overnight in low-serum medium with  $1 \mu\text{M}$  SAG21k (to induce SMO activation and ciliary accumulation.) A previously described cell line coexpressing mNeonGreen-tagged Nb $\beta$ 2AR80 with wild-type FLAG-tagged SMO<sup>29</sup> was used as a negative control. Live cells were subsequently stained for 5–10 min with an Alexa647-conjugated M1 anti-FLAG antibody (1:1,000) and Hoechst counterstain, followed by washing in Hank's buffered saline solution, mounting and visualization. Cells were imaged on a Leica SP8 laser scanning confocal using a  $\times 40$  water immersion lens. Three-dimensional reconstructions of Z-stacks were performed in Fiji using the 3D Viewer plugin. Quantification of SMO (red) and PKA-C/Nb $\beta$ 2AR80 (green) staining was performed using CiliaQ<sup>111</sup> and reported as a ratio of the green fluorescence in each cilium, normalized to the red fluorescence (Colocalization with SMO in cilia (a.u.)), as previously described<sup>29</sup>. All images were acquired with identical zoom/exposure/gain settings. The imaging was repeated on multiple occasions and all data were pooled together to generate the plots/quantification in the relevant figure panels.

### Immunofluorescence microscopy in NIH3T3 Flp-in cells

NIH3T3 cell lines stably expressing mSmo-V5-TurboID were generated using the Flp-in system following the manufacturer's instructions. Briefly, Flp-in NIH3T3 cells were cotransfected with pEF5-FRT-mSmo-V5-TurboID and Flp recombinase expressing plasmid pOG44 with Lipofectamine 2000 reagent. Cells were selected with  $0.2 \text{ mg ml}^{-1}$  hygromycin. Single colonies were expanded and protein expression was confirmed by immunoblotting, immunofluorescence microscopy and quantitative PCR. A cell clone that expressed low levels of SMO and displayed strong SAG-induced accumulation of SMO in cilia was chosen and expanded for further study.

mSmo-V5-TurboID stable cells were grown on poly-D-lysine-coated 12 mm no. 1.5 coverslips. Once reaching 80–90% confluency, cells were treated with low-serum medium (DMEM + 0.5% FBS) or low-serum medium +  $100 \text{ nM}$  SAG/ $5 \mu\text{M}$  Cyclopamine for the indicated times.

Live cells were subsequently incubated with  $500 \mu\text{M}$  Biotin for 15 min at  $37^\circ\text{C}$ , 5%  $\text{CO}_2$  and washed once with Dulbecco's PBS before fixation in 4% PFA. Cells were blocked with blocking buffer (0.2% Triton X-100, 2% Donkey serum in PBS) for 1 h at room temperature. Cells were first stained with rabbit anti-ARL13B (1:1,000) and mouse anti-PKA-C (1:200) overnight at  $4^\circ\text{C}$ . Subsequently, cells were incubated with Rhodamine antirabbit (1:100), Alexa 488 antimouse (1:200) and Alexa647 streptavidin (1:200) for 1 h at room temperature followed by Hoechst 33342 staining and mounting.

Imaging was performed with a LEICA DMi8 system with  $\times 63$  oil-immersion lens. Quantification of SMO and PKA-C staining was performed in Fiji. Briefly, the contour of the cilium was outlined in Arl13b channel, and the intensity within the area of interest was measured in SMO and PKA-C channels. After that the contour was dragged to the nearby area immediately adjacent to the cilium to measure the background values, which were then subtracted from the cilium intensity. The intensities are reported in a.u.

### GLI reporter assays

GLI transcriptional reporter assays were performed as previously described<sup>29</sup>. Briefly, *Smo*<sup>-/-</sup> MEFs were transfected with a 30:1 mixture of 8xGli-Firefly and SV40-Renilla plasmids (50% (w/w)), along with the indicated full-length wild-type or mutant SMO constructs (in a pGEN vector, with C-terminal myc tag) (2% (w/w)) and GFP to adjust the amount of DNA to 250 ng per well. Cells were cultured to confluency, shifted to 0.5% FBS-containing medium and treated with control or ShhN conditioned medium (1:20 dilution) for 2 days. Reporter activity was then measured via dual-luciferase assay. For all GLI assays, data represent mean  $\pm$  s.d. from triplicate wells and data are representative of at least two independent experiments.

### Zebrafish embryological studies

Zebrafish mRNA injection, fixing, mounting and staining of muscle cell markers were all performed on *Danio rerio* embryos (both males and females) derived from *Tubingen* strain adult zebrafish (<26 h post-fertilization) kept on a light–dark cycle of 14 h in light and 10 h in dark at  $27^\circ\text{C}$ , using anti-Prox1 (1:1,000) and anti-Engrailed (1:5) as previously described<sup>29</sup>, except that a far-red secondary antibody (donkey antirabbit 649, Jackson Laboratory, 1:500) was used instead of a red secondary antibody during immunohistochemistry. Zebrafish (*D. rerio*) were maintained in accordance with approved institutional protocols at the University of Utah. Specifically, all experimental protocols were approved by the University of Utah Institutional Animal Care and Use Committee and were in accordance with the guidelines from the National Institutes of Health (approval number 19–11006). The numbers of animals used in each experiment are indicated in the corresponding figure or table legends.

### Software

Microscopy data were acquired using Application Suite X v.3.5.7 (Leica) and analyzed using Fiji v.2.3.0. SDS–PAGE and western blots were acquired using Image Lab v.6.1.0 (BioRad). BRET measurements were acquired using SparkControl v.2.2 (Tecan). SPR data were acquired and analyzed using Biacore T200 Evaluation Software 3.0 (Cytiva). Multi-angle light scattering data were acquired using Astra v.8.0 (Wyatt). Flow cytometry data were acquired using CytExpert v.2.3.1.22 (Beckman Coulter) and analyzed using FlowJo v.10.8.1. NMR data were analyzed using NMRpipe 8 and NMRFAM-SPARKY v.1.3. Protein Data Bank (PDB) files were viewed using Pymol v.2.4.2. Graphs, curve fitting and statistical analysis were performed in GraphPad Prism v.9.3.1. Alignments were generated using CLUSTAL Omega v.1.2.2. Graphics were generated using BioRender or Adobe Illustrator 2021.

### Statistics and reproducibility

All statistics used GraphPad Prism (v.9.3.1) unless stated otherwise, using *t*-tests or analyses of variance as indicated in Supplementary

**Table 1.** No statistical method was used to predetermine sample size. However, we used similar numbers of cells and animals to previous studies in our field that used these experimental models. All experiments shown were reproduced on at least two independent occasions. For all statistical analyses, *n* reflects the number of independent experimental or biological replicates. No data were excluded from the analyses. Randomization and blinding methods were not used.

### Reporting summary

Further information on research design is available in the Nature Research Reporting Summary linked to this article.

### Data availability

Source data, including uncropped gels and western blots, are provided with this paper. All unique biological materials are available on request from the authors.

### References

- Zimmermann, B., Schweinsberg, S., Drewianka, S. & Herberg, F. W. Effect of metal ions on high-affinity binding of pseudosubstrate inhibitors to PKA. *Biochem. J.* **413**, 93–101 (2008).
- Myers, B. R. et al. Hedgehog pathway modulation by multiple lipid binding sites on the Smoothed effector of signal response. *Dev. Cell* **26**, 346–357 (2013).
- Lu, T. W. et al. Two PKA RI $\alpha$  holoenzyme states define ATP as an isoform-specific orthosteric inhibitor that competes with the allosteric activator, cAMP. *Proc. Natl Acad. Sci. USA* **116**, 16347–16356 (2019).
- Olsen, S. R. & Uhler, M. D. Affinity purification of the C $\alpha$  and C $\beta$  isoforms of the catalytic subunit of cAMP-dependent protein kinase. *J. Biol. Chem.* **264**, 18662–18666 (1989).
- Walker, C. et al. Cushing's syndrome driver mutation disrupts protein kinase A allosteric network, altering both regulation and substrate specificity. *Sci. Adv.* **5**, eaaw9298 (2019).
- Walsh, D. A. & Ashby, C. D. Protein kinases: aspects of their regulation and diversity. *Recent Prog. Horm. Res* **29**, 329–359 (1973).
- Manu, V. S., Olivieri, C., Pavuluri, K. & Veglia, G. Design and applications of water irradiation devoid RF pulses for ultra-high field biomolecular NMR spectroscopy. *Phys. Chem. Chem. Phys.* **24**, 18477–18481 (2022).
- Delaglio, F. et al. NMRPipe: a multidimensional spectral processing system based on UNIX pipes. *J. Biomol. NMR* **6**, 277–293 (1995).
- Lee, W., Tonelli, M. & Markley, J. L. NMRFAM-SPARKY: enhanced software for biomolecular NMR spectroscopy. *Bioinformatics* **31**, 1325–1327 (2015).
- Williamson, M. P. Using chemical shift perturbation to characterise ligand binding. *Prog. Nucl. Magn. Reson. Spectrosc.* **73**, 1–16 (2013).
- Hansen, J. N., Rassmann, S., Stuken, B., Jurisch-Yaksi, N. & Wachten, D. CiliaQ: a simple, open-source software for automated quantification of ciliary morphology and fluorescence in 2D, 3D, and 4D images. *Eur. Phys. J. E Soft Matter* **44**, 18 (2021).

### Acknowledgements

We thank J. Zalatan for making us aware of the parallels between SMO/PKA-C regulation in the Hh pathway and LRP/GSK-3 $\beta$  regulation in the Wnt pathway. We thank S. Lusk and K. Kwan (University of Utah) for providing *smo*-null zebrafish (*smo*<sup>h1640</sup>), and D. Klatt Shaw and D. Grunwald (University of Utah) for sharing advice and reagents

regarding zebrafish immunohistochemistry. We thank J. Müller and S. Kasten (University of Kassel) for excellent technical assistance. We thank the Johnson Foundation Structural Biology and Biophysics Core at the Perelman School of Medicine (University of Pennsylvania, Philadelphia, PA, USA) for performing multi-angle light scattering coupled with size-exclusion chromatography analyses. We thank D. Julius, S. Nakielny, A. Manglik, K. Basham and M. He for providing feedback on the manuscript. B.R.M. acknowledges support from the 5 for the Fight Foundation (award no. 6000-32705) and a Cancer Center Support Grant Pilot Project Fund from the Huntsman Cancer Institute (award no. 200206). This work was supported by the DFG (the German Research Foundation) grant no. GRK2749/1 (F.W.H.) and National Institutes of Health grant nos. R01GM100310-08 (G.V.), 1R35GM130389 (S.S.T.), 1R03TR002947 (S.S.T.) and 1R35GM133672 (B.R.M.).

### Author contributions

J.T.H. designed, executed and interpreted CREB and GLI reporter assays. C.D.A. designed, executed and interpreted HEK293 BRET assays. J.B. designed, executed and interpreted fluorescence polarization studies and peptide array studies. D.B., J.W.B. and F.W.H. designed, executed and interpreted in vitro PKA-C activity assays and SPR studies. I.B.N. developed SMO pCT purification approaches and purified this domain for in vitro PKA-C activity assays. C.O. designed, executed and interpreted NMR studies. J.Z. designed, executed and interpreted all NIH3T3 imaging studies, under supervision from X.G. D.S.H. designed, executed and interpreted zebrafish embryology studies. J.-F.Z. designed, executed and interpreted coimmunoprecipitation and IMCD3 BRET assays. J.L.C. designed, executed and interpreted HEK293 confocal imaging studies. L.V. performed initial fluorescence polarization studies. C.C.K. collaborated with J.B. to develop SMO peptide arrays. V.L.R.-P. provided advice and guidance on mutagenesis experiments to disrupt SMO-PKA-C interactions. S.S.T. and B.R.M. conceived the project. G.V., F.W.H., S.S.T. and B.R.M. interpreted data and provided overall project supervision. B.R.M. performed IMCD3 ciliary imaging studies and wrote the manuscript with assistance from J.T.H., C.D.A. and I.B.N.

### Competing interests

The authors declare no competing interests.

### Additional information

**Extended data** are available for this paper at <https://doi.org/10.1038/s41594-022-00838-z>.

**Supplementary information** The online version contains supplementary material available at <https://doi.org/10.1038/s41594-022-00838-z>.

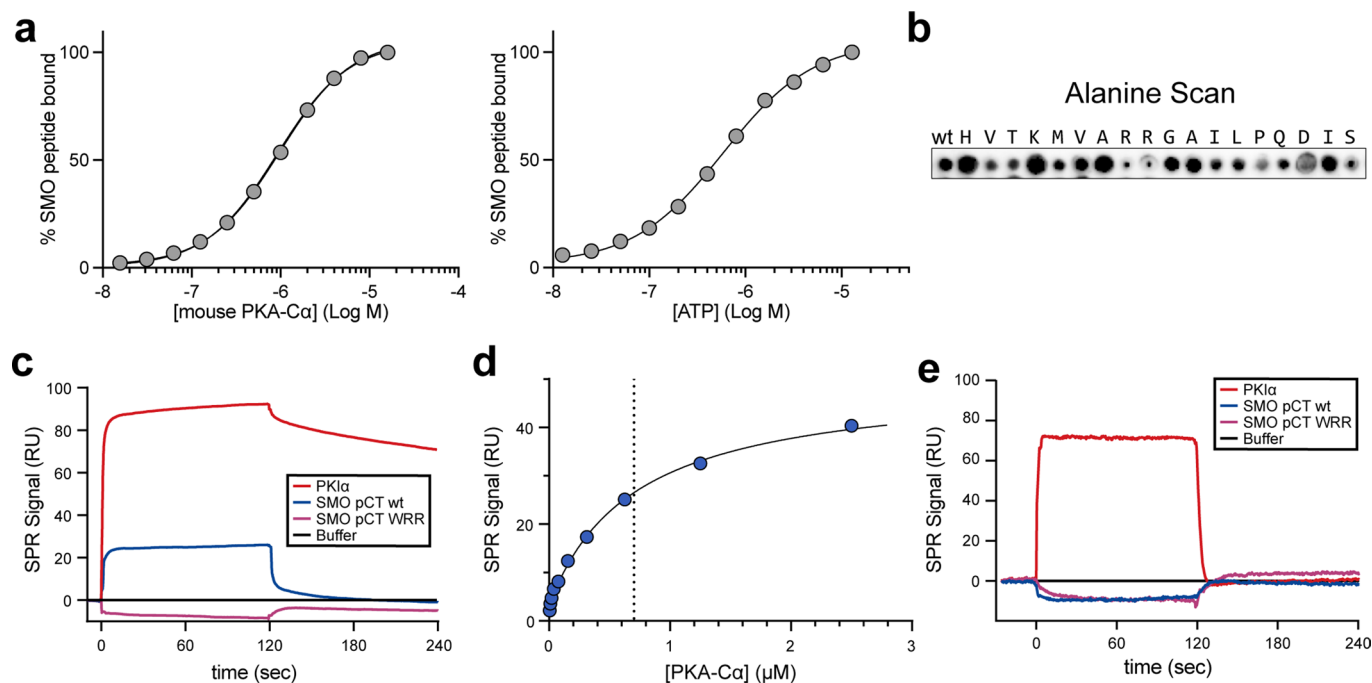
**Correspondence and requests for materials** should be addressed to Susan S. Taylor or Benjamin R. Myers.

**Peer review information** *Nature Structural & Molecular Biology* thanks Philip Ingham and the other, anonymous, reviewer(s) for their contribution to the peer review of this work. Primary Handling Editors: Carolina Perdigoto, Beth Moorefield and Anke Sparmann in collaboration with the *Nature Structural & Molecular Biology* team.

**Reprints and permissions information** is available at [www.nature.com/reprints](http://www.nature.com/reprints).

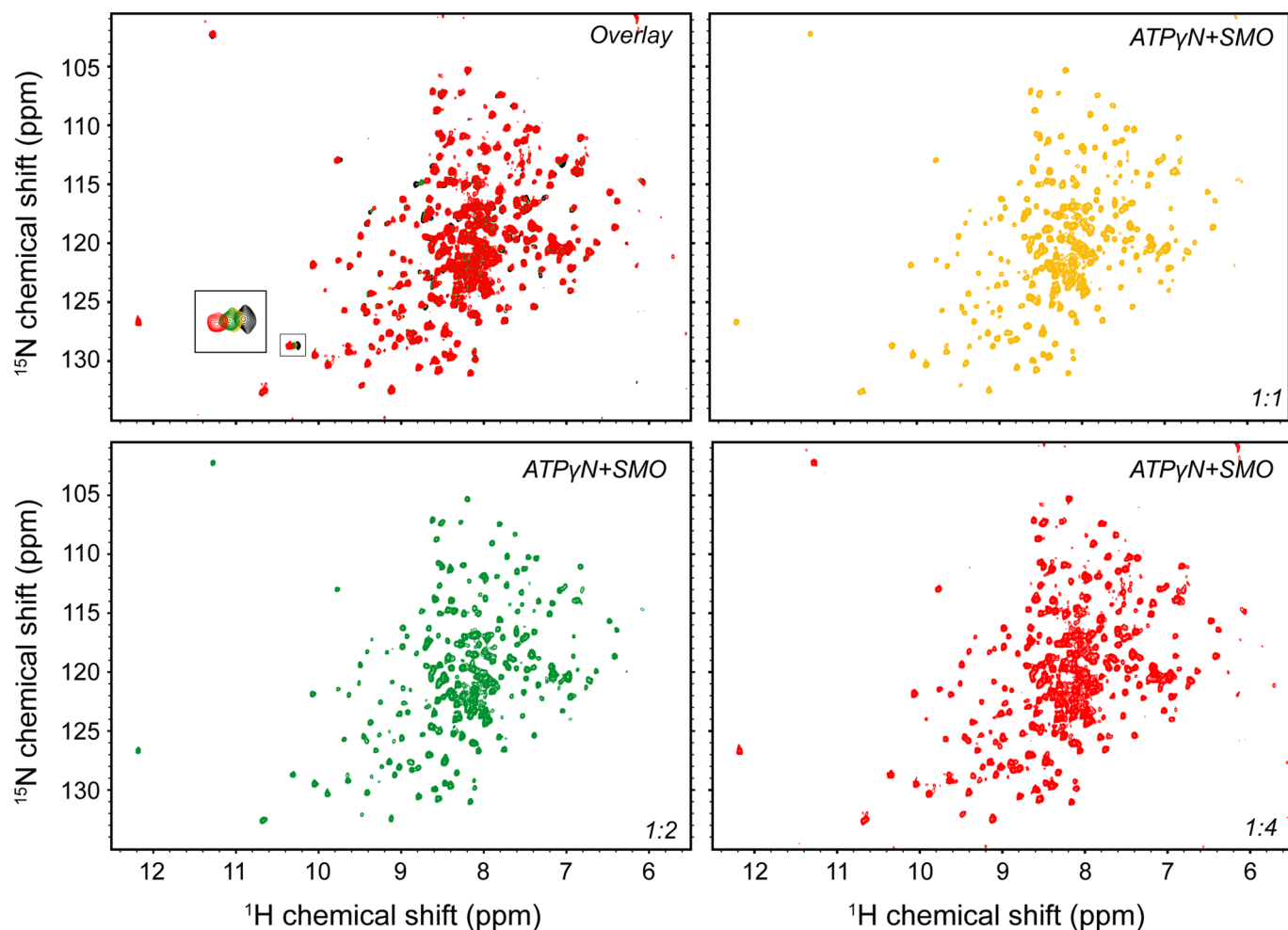
		P-13	P-3	P-2	P	P-1	
Mus_musculus	AGLAFDLNEPS-----ADVSSAWAQHV-TKMVARRGAILPQDVS-VTPVATPVPP---EE						654
Homo_sapiens	AGLAFDLNEPS-----ADVSSAWAQHV-TKMVARRGAILPQDIS-VTPVATPVPP---EE						650
Danio_erio	AGINFDLNEPS-----IEMSSAWAQHV-TKMVARRGAILPQDIS-VTPTGTPIPP--PEE						630
Xenopus_laevis	AGLNFDLNEPS-----ADMSSAWAQHV-TKMVARRGAILPQDVS-VTPVATPVPP---EE						623
Gallus_gallus	AGLAFDINEPS-----ADVSSAWAQHV-TKMVARRGAILPQDVS-VTPVATPVPP---EE						517
Drosophila_melanogaster	VGLNFDVNDLNS-SETNDISSTWAAYL-PQCVKRRMALTGAATGNSSSH-GPRKNSLDSE						671
Ciona_intestinalis	LGMNFDLHSVS-----QEMSSWVRNV-PNMVKRRGGMLPMEQPHDNVE-----						611
Lytechinus_variegatus	IGMKLDLPPSSVVGDDPTSSSSWGNNVPVRMLARRGAAYPIATLGNSPRATPDSS--DSG						641
Petromyzon_marinus	VGMDLNLDDSG-----S-DSSSWINHV-TKMVARRGAILP-----						581
Novocrania_anomala	LGMKFDLNSVT----SQDMSSAWMEAV-PRLVRRRGGMIHPTAGTLRRYSDS-----DI						621

**Extended Data Fig. 1 | Sequence alignment of SMO PKI motif.** Extended alignment of a portion of the pCT from the indicated SMO orthologs, with key PKI motif residues colored as in Fig. 1a.



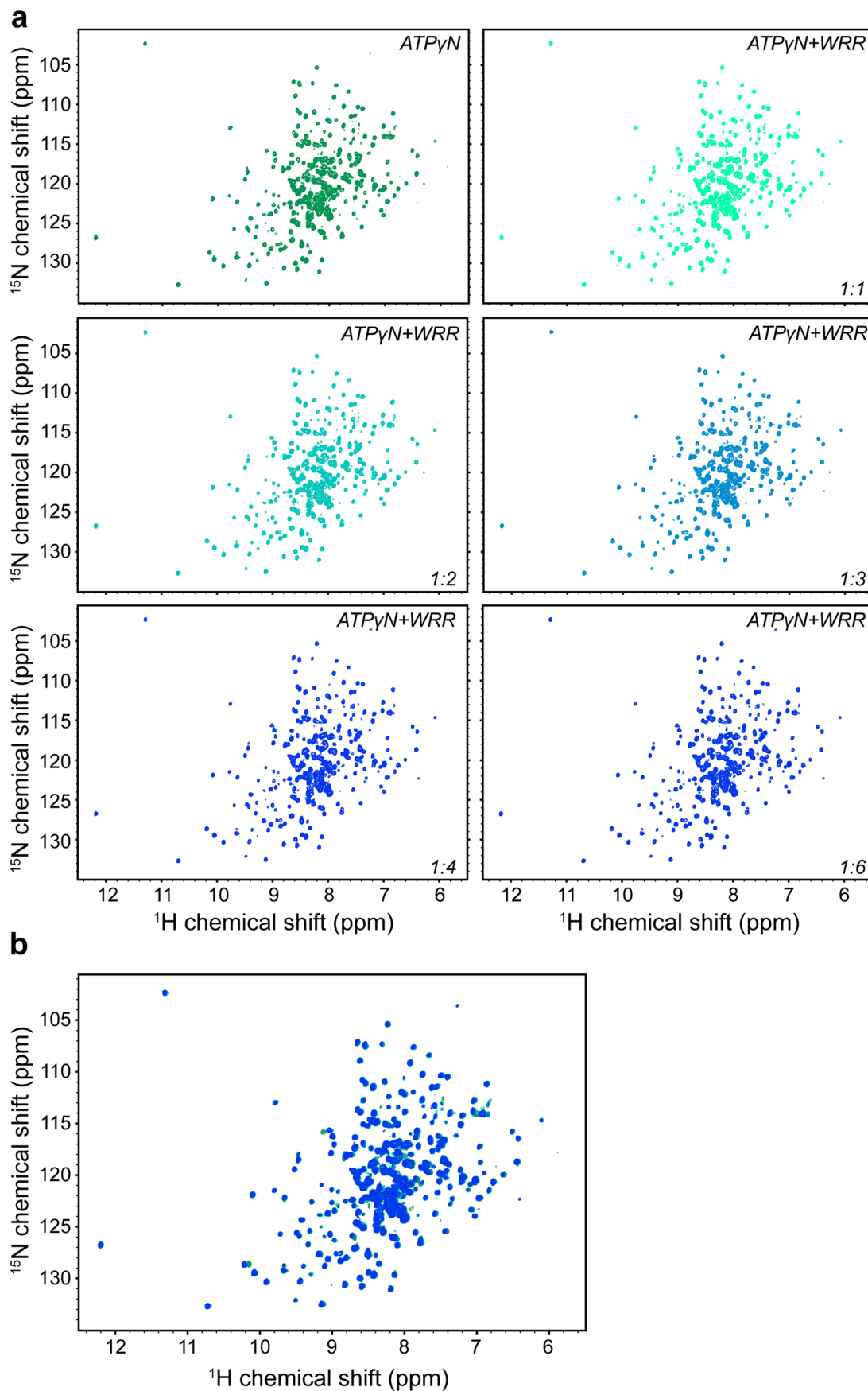
**Extended Data Fig. 2 | Additional binding and peptide array studies, and SPR sensorgrams. a**, Fluorescence polarization assays using mouse PKA-C $\alpha$ , performed as in Fig. 1b. Triplicate points from representative experiments are shown. **b**, Peptide array, performed as in Fig. 1c, but with individual residues in the human SMO PKI motif mutated to alanine. **c**, SPR sensorgram for 625 nM PKA-C $\alpha$  binding to GST-tagged wild-type (blue) or WRR mutant (purple) SMO pCT, or a PKI $\alpha$  positive control (red), in the presence of ATP and MgCl $_2$ . **d**, Exemplary steady-state analysis of binding interactions between human PKA-C $\alpha$  and a

recombinant wild-type SMO pCT, with a  $K_D$  of 703  $\pm$  0.003 nM (dotted line) as assessed by SPR. This measurement was made three times, resulting in a mean  $K_D$  value of 752  $\pm$  34 nM. **e**, SPR sensorgram, performed as in c, but with ATP and MgCl $_2$  omitted from the buffer. PKA-C $\alpha$  was present at 2.5  $\mu$ M. Note that although removal of ATP and MgCl $_2$  does not completely eliminate steady-state binding to the PKI $\alpha$  positive control, it dramatically accelerates the dissociation rate, as expected.



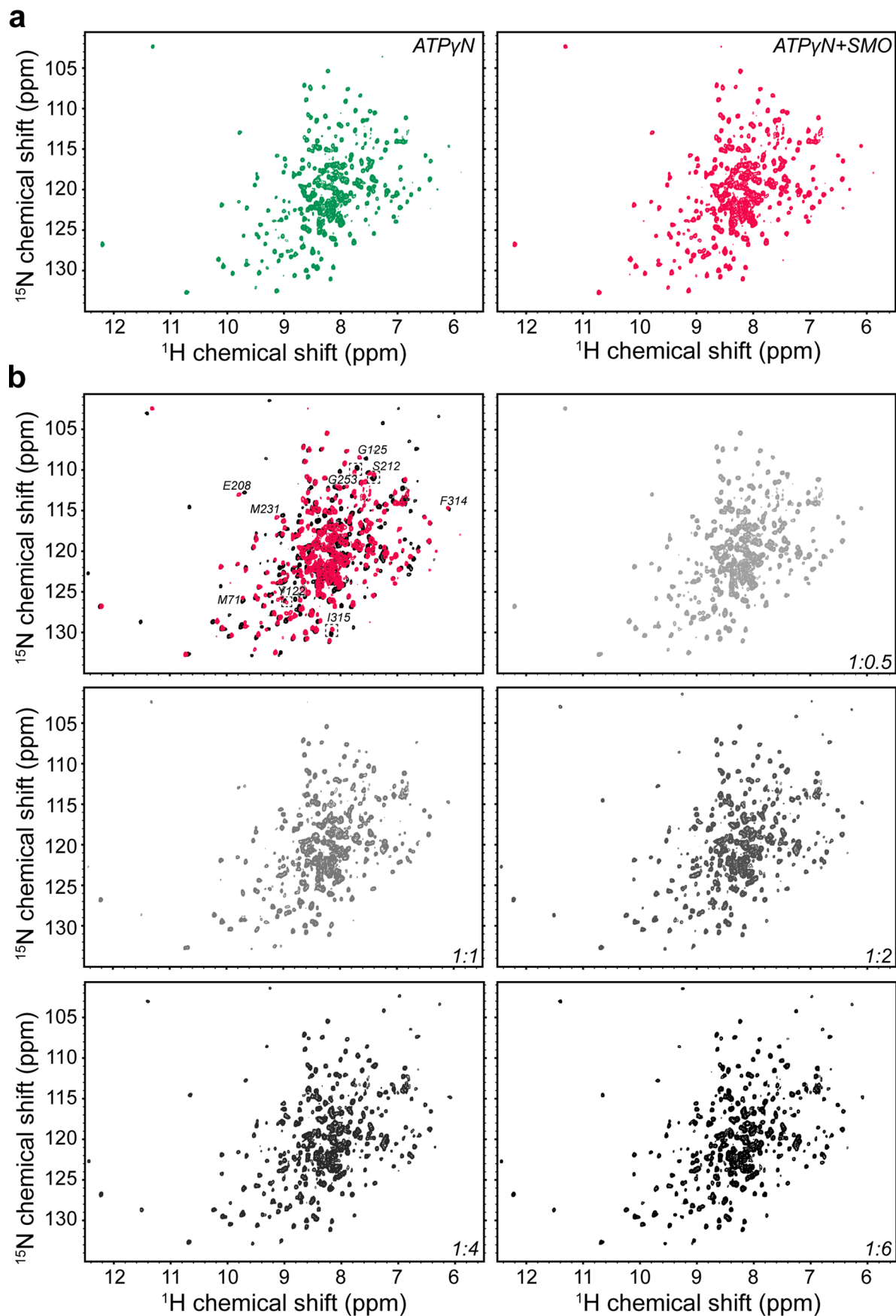
**Extended Data Fig. 3 | Raw NMR spectra for wild-type SMO peptide binding to PKA-C $\alpha$  at varying kinase:peptide ratios.** 2D NMR spectra from an experiment in which SMO peptide was titrated into ATP $\gamma$ N-bound PKA-C $\alpha$  at the indicated kinase:peptide ratios. Upper left panel represents an overlay of all three spectra to highlight the concentration dependence of the SMO peptide-induced

changes observed in each spectrum. Black spectrum represents ATP $\gamma$ N-bound PKA-C $\alpha$  without SMO peptide (see also Extended Data Figs. 4, 5). In the overlay plot, a box denotes one example of a peak (likely corresponding to an unassigned tryptophan residue) that changes linearly according to SMO peptide concentration (magnified in the inset at left).



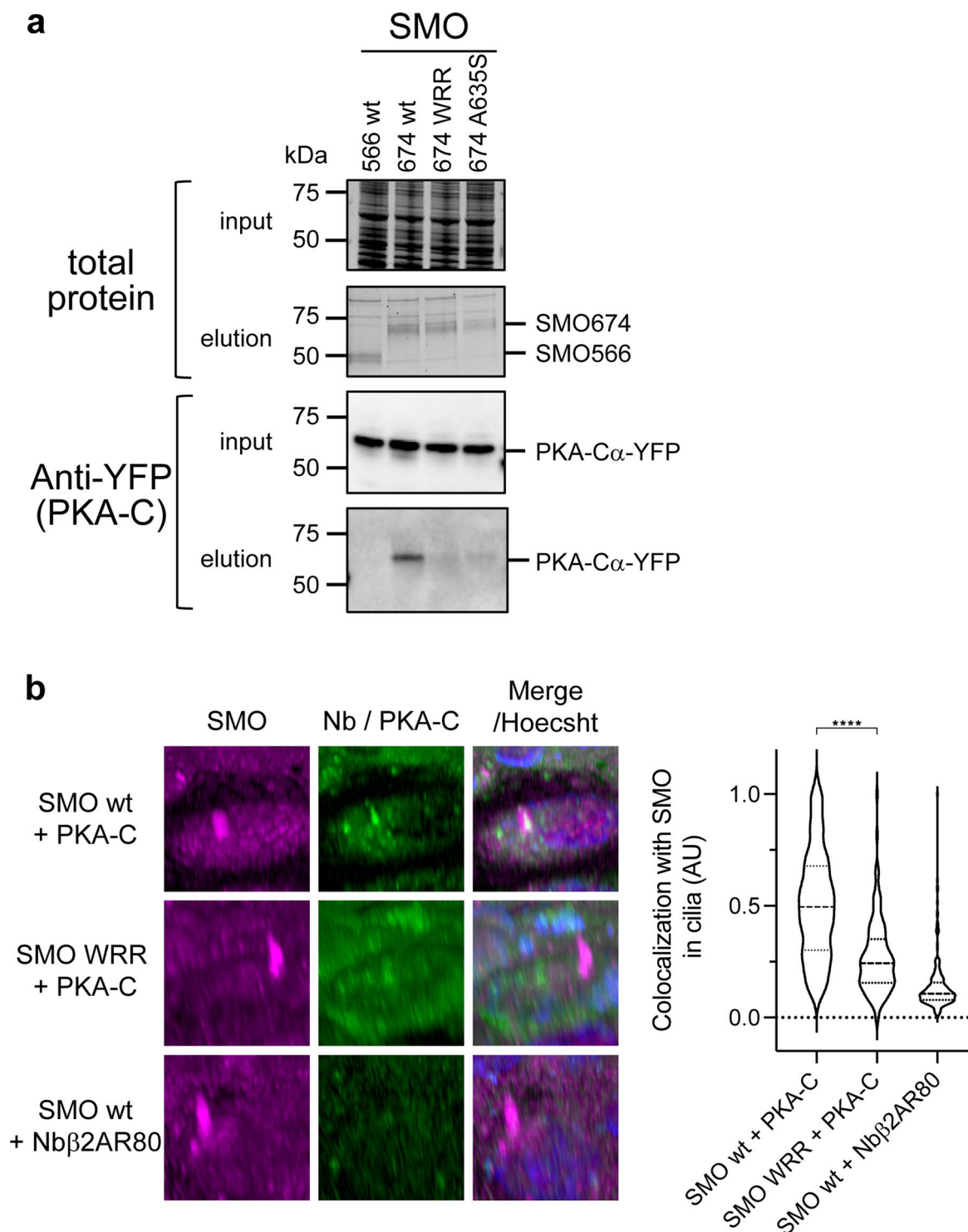
**Extended Data Fig. 4 | Raw NMR spectra for WRR mutant peptide binding to PKA-C $\alpha$ , as shown in Fig. 2a. a.** The WRR mutant SMO peptide was titrated into ATP $\gamma$ N-bound PKA-C $\alpha$  at the indicated kinase:peptide ratios. ATP $\gamma$ N-bound

PKA-C $\alpha$  without peptide (dark green spectrum, upper left) is shown for reference. See Extended Data Fig. 5 for raw NMR spectrum corresponding to ATP $\gamma$ N-bound PKA-C $\alpha$ :wild-type SMO peptide at 1:6 ratio. **b.** Overlay of the spectra in **a**.



**Extended Data Fig. 5 | Raw NMR spectra for wild-type SMO peptide binding to PKA-C $\alpha$ , as shown in Fig. 2a, and PKI $\alpha$ (5-24)-induced displacement of SMO peptide from PKA-C $\alpha$ , as shown in Fig. 2c. **a**, 2D NMR spectra for ATP $\gamma$ N-bound PKA-C $\alpha$ , either alone (left) or with SMO peptide added at a 1:6 kinase:peptide**

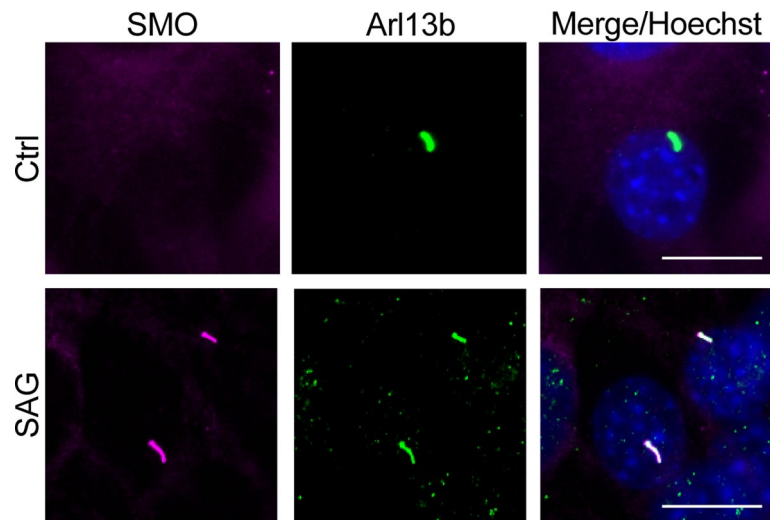
**ratio (right). **b****, 2D NMR spectra for titration of PKI $\alpha$ (5-24) peptide into the SMO peptide:ATP $\gamma$ N:PKA-C $\alpha$  complex at the indicated kinase:PKI $\alpha$ (5-24) ratios. Upper left panel represents an overlay of the individual spectra to highlight the concentration dependence of the PKI $\alpha$ (5-24) peptide-induced effects.



**Extended Data Fig. 6 | Coimmunoprecipitation studies and ciliary colocalization studies to assess SMO / PKA-C interactions.**

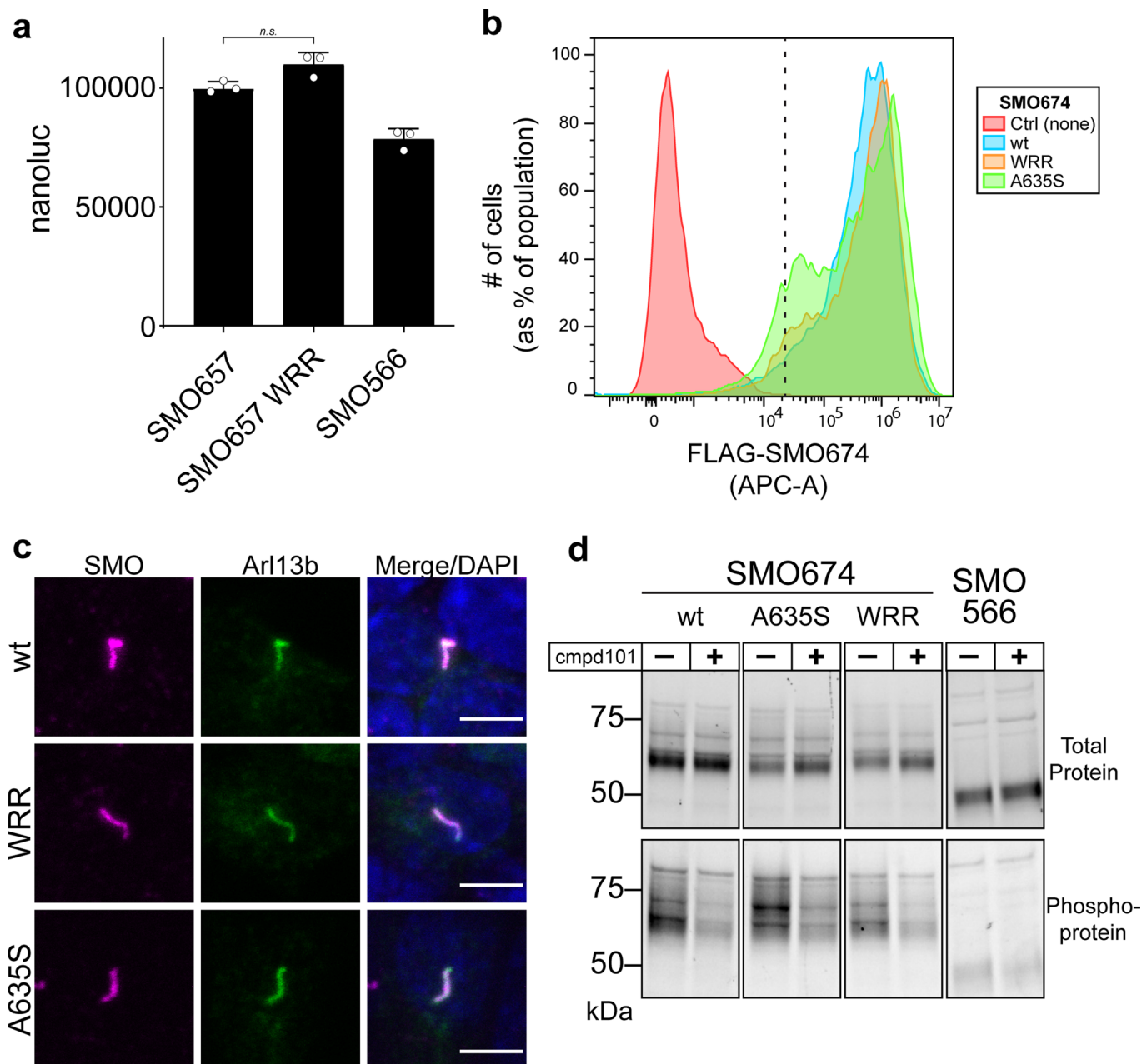
**a**, Coimmunoprecipitation of PKA-C $\alpha$ -YFP with the indicated FLAG-tagged wild-type or mutant SMO constructs was assessed using FLAG chromatography from lysates of transfected HEK293 cells. Data shown are representative of two independent experiments. **b**, Left, Colocalization of FLAG-tagged wild-type or mutant SMO674 (magenta) with mNeonGreen-tagged PKA-C $\alpha$  (green) in ciliated IMCD3 cells stably expressing both constructs and treated with the SMO

agonist SAG21k. Cilia are marked by the SMO (FLAG-647) stain. mNeonGreen-tagged Nb $\beta$ 2AR80 (which does not bind SMO<sup>29</sup>) serves as a negative control. 3D reconstructions from Z-stacks of confocal live-cell images are shown. Right, quantification of microscopy studies with the median represented by a dashed line and the upper and lower quartiles indicated by dotted lines ( $n = 142$ – $244$  cilia per condition).  $P < 0.0001$  (\*\*\*\*). See Supplementary Table 1 for full statistical analysis.



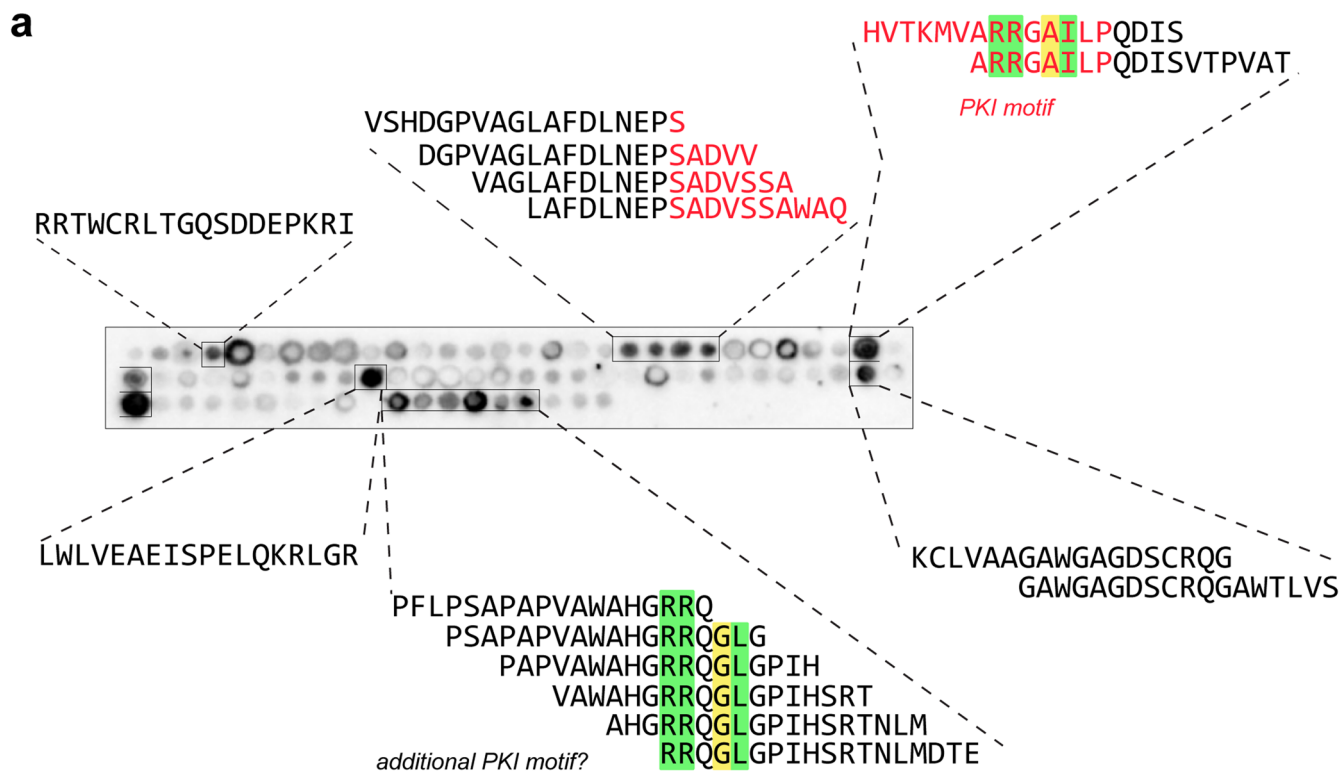
**Extended Data Fig. 7 | Characterization of NIH3T3 cell line expressing epitope-tagged SMO.** The NIH3T3 cell line used in Fig. 5 exhibited trace amounts of SMO in cilia under vehicle ('Ctrl')-treated conditions, and a dramatic accumulation of SMO in cilia under SAG-treated conditions. SMO (magenta) is

visualized using an anti-V5 antibody, and cilia are visualized using an anti-Arl13b antibody (green). Scale bar = 10  $\mu\text{m}$ . Data shown are representative of two independent experiments.



**Extended Data Fig. 8 | Controls for SMO/PKA-Cbinding, colocalization, and signaling studies.** **a**, Expression levels of SMO constructs in Fig. 3a, assessed by whole-cell nanoluc measurements. Data represent the mean  $\pm$  standard deviation,  $n = 3$  biologically independent samples. NS = not significant. **b**, Surface levels of N-terminally FLAG-tagged wild-type or mutant SMO674 constructs were quantified via expression in HEK293 cells followed by FLAG staining and flow cytometry. Mock-infected cells stained with FLAG antibody (red) serve as a negative control. A representative histogram is shown. The % of FLAG-positive cells (that is, those to the right of the vertical dashed line) are:  $0.3 \pm 0.3\%$  (Ctrl);  $95.9 \pm 0.9\%$  (wt);  $96.0 \pm 2.5\%$  (WRR);  $93.4 \pm 4.2\%$  (A635S); values represent the mean  $\pm$  standard deviation from two biologically independent samples. See Supplementary Table 1 for full statistical analysis, and

Supplementary Figure 2 for gating strategy. **c**, Ciliary localization in IMCD3 cells of myc-tagged wild-type or mutant SMO proteins (magenta). Cilia were visualized with Arl13b antibody (green). Scale bar =  $5 \mu\text{m}$ . Data shown are representative of two independent experiments. **d**, GRK2/3-dependent phosphorylation of FLAG-tagged wild-type or mutant SMO674 constructs was determined via expression in HEK293 cells treated with or without the GRK2/3 inhibitor cmpd101, followed by FLAG purification. Levels of total and phosphorylated SMO were assessed by Stain Free imaging and ProQ Diamond fluorescence, respectively. SMO566, which is not phosphorylated by GRK2/3 (as it does not contain the C-tail and therefore lacks all previously mapped physiological GRK2/3 phosphorylation sites), serves as a negative control. Data shown are representative of two independent experiments.

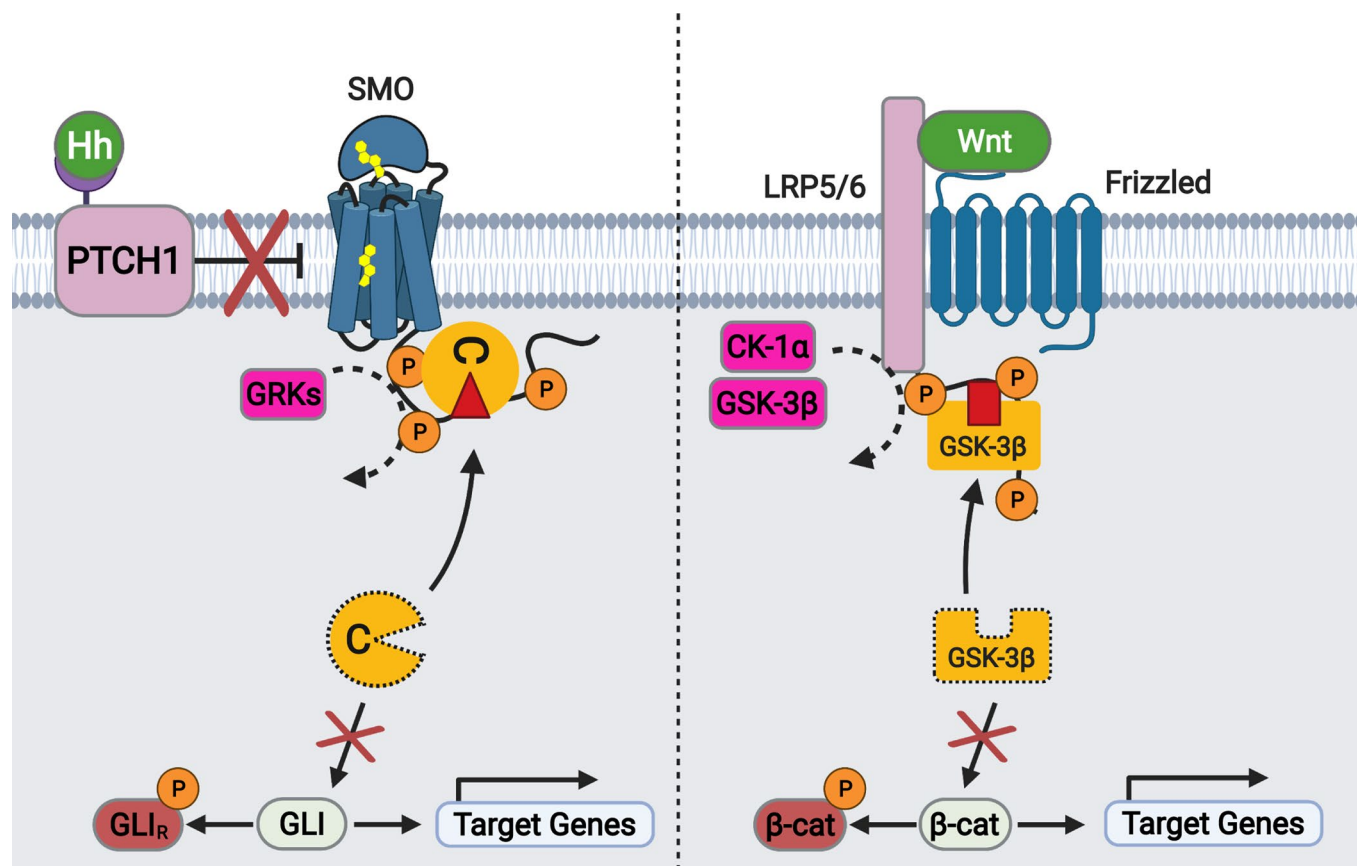


**b** Human SMO C-tail

<sup>535</sup> WTKATLLIWRRTWCRLTGQSDDEPKRIKKSKMIAKAFSKRHELLQNPQGELSFSM  
HTVSHDGPVAGLAFDLNEP **SADVSSAWAQHVTKMVARRGAILPQDISVTPVATPVPPE**  
EQANLWLVEAEISPELQKRLGRKKRKRKKEVCPLAPPELHPPAPAPSTIPRLPQL  
PRQKCLVAAGAWGAGDSCRQGAWTLVSNPFCPEPSPQDPFLPSAPAPVAWAHGRRQG  
LGPIHSRTNLMDELMDADSSDF <sup>786</sup>

**Extended Data Fig. 9 | Complete data set from SMO C-tail peptide array studies. a.** The same SMO tiled peptide array from Fig. 7c, but including the sequences of all positive hits in each array cluster. **b.** Complete human SMO C-tail

sequence used to create the peptide array. In **a, b**, the SMO PKI motif identified in the pCT is indicated in red. Key residues in this PKI motif, along with ones in the candidate PKI motif in the dCT, are colored as in Fig. 1a.



**Extended Data Fig. 10 | Similarity between signal transduction mechanisms in the Hh and Wnt pathways.** Schematic diagram of transmembrane signal transduction in the Hh (left) and Wnt (right) pathways. During Hh signal transduction, active SMO is phosphorylated on its cytoplasmic tail by GRK2/3, triggering membrane sequestration and inhibition of PKA-C, and ultimately stabilization and activation of GLI. During Wnt signal transduction, active LRP5/6 is phosphorylated on its cytoplasmic tail by glycogen synthase kinase (GSK)-3β

and casein kinase (CK)-1α, triggering membrane sequestration and inhibition of GSK-3β, and ultimately stabilization and activation of β-catenin. Note that this is a simplified and highly schematized diagram and is not intended to be comprehensive; many other components of both pathways (for example, the destruction complex in which GSK-3β and β-catenin reside) are omitted in order to highlight mechanistic similarities between the underlying transmembrane signaling mechanisms.

## Reporting Summary

Nature Portfolio wishes to improve the reproducibility of the work that we publish. This form provides structure for consistency and transparency in reporting. For further information on Nature Portfolio policies, see our [Editorial Policies](#) and the [Editorial Policy Checklist](#).

### Statistics

For all statistical analyses, confirm that the following items are present in the figure legend, table legend, main text, or Methods section.

n/a Confirmed

- The exact sample size ( $n$ ) for each experimental group/condition, given as a discrete number and unit of measurement
- A statement on whether measurements were taken from distinct samples or whether the same sample was measured repeatedly
- The statistical test(s) used AND whether they are one- or two-sided  
*Only common tests should be described solely by name; describe more complex techniques in the Methods section.*
- A description of all covariates tested
- A description of any assumptions or corrections, such as tests of normality and adjustment for multiple comparisons
- A full description of the statistical parameters including central tendency (e.g. means) or other basic estimates (e.g. regression coefficient) AND variation (e.g. standard deviation) or associated estimates of uncertainty (e.g. confidence intervals)
- For null hypothesis testing, the test statistic (e.g.  $F$ ,  $t$ ,  $r$ ) with confidence intervals, effect sizes, degrees of freedom and  $P$  value noted  
*Give  $P$  values as exact values whenever suitable.*
- For Bayesian analysis, information on the choice of priors and Markov chain Monte Carlo settings
- For hierarchical and complex designs, identification of the appropriate level for tests and full reporting of outcomes
- Estimates of effect sizes (e.g. Cohen's  $d$ , Pearson's  $r$ ), indicating how they were calculated

*Our web collection on [statistics for biologists](#) contains articles on many of the points above.*

### Software and code

Policy information about [availability of computer code](#)

**Data collection** Leica Application Suite X 3.5.7 (imaging acquisition), Biorad ImageLab 6.1.0 (SDS-PAGE, western blots), Tecan SparkControl 2.2 (BRET measurements), Biacore T200 Evaluation Software 3.0 (SPR), Astra 8.0 software (MALS), CytExpert 2.3.1.22 (flow cytometry data collection)

**Data analysis** GraphPad Prism 9.3.1 (graphs, statistical analysis), FlowJo 10.8.1 (analysis of FACS data), Fiji 2.3.0 (imaging analysis), Pymol 2.4.2 (PDB visualization), NMRPipe 8 (NMR data), NMRFAM-SPARKY 1.3 (NMR data), CLUSTAL Omega 1.2.2 (sequence alignments)

For manuscripts utilizing custom algorithms or software that are central to the research but not yet described in published literature, software must be made available to editors and reviewers. We strongly encourage code deposition in a community repository (e.g. GitHub). See the Nature Portfolio [guidelines for submitting code & software](#) for further information.

### Data

Policy information about [availability of data](#)

All manuscripts must include a [data availability statement](#). This statement should provide the following information, where applicable:

- Accession codes, unique identifiers, or web links for publicly available datasets
- A description of any restrictions on data availability
- For clinical datasets or third party data, please ensure that the statement adheres to our [policy](#)

Source data, including uncropped gels and Western blots, are provided with this paper. All unique biological materials are available upon request from the authors.

## Field-specific reporting

Please select the one below that is the best fit for your research. If you are not sure, read the appropriate sections before making your selection.

Life sciences       Behavioural & social sciences       Ecological, evolutionary & environmental sciences

For a reference copy of the document with all sections, see [nature.com/documents/nr-reporting-summary-flat.pdf](https://www.nature.com/documents/nr-reporting-summary-flat.pdf)

## Life sciences study design

All studies must disclose on these points even when the disclosure is negative.

Sample size	No statistical methods were used to pre-determine sample size. Sample sizes were determined based on our extensive prior experience and are standard for peer-reviewed studies in our field. The size of each sample (n) is reported in the relevant Figure Legend or in the Method section.
Data exclusions	No data were excluded.
Replication	All results were replicated in at least two independent experiments performed on two separate occasions. All attempts at replication were successful.
Randomization	All experiments were initiated from multiple independent pools of transfected cells derived from the same frozen vial of cells, and then subjected to indicated experimental conditions. Randomization was not applicable to our study, as is standard for biochemical, cultured cell, and embryological assays in our field.
Blinding	Blinding was not applicable to our study, as is standard for biochemical, cultured cell, and embryological assays in our field.

## Reporting for specific materials, systems and methods

We require information from authors about some types of materials, experimental systems and methods used in many studies. Here, indicate whether each material, system or method listed is relevant to your study. If you are not sure if a list item applies to your research, read the appropriate section before selecting a response.

### Materials & experimental systems

### Methods

n/a	Involved in the study
<input type="checkbox"/>	<input checked="" type="checkbox"/> Antibodies
<input type="checkbox"/>	<input checked="" type="checkbox"/> Eukaryotic cell lines
<input checked="" type="checkbox"/>	<input type="checkbox"/> Palaeontology and archaeology
<input type="checkbox"/>	<input checked="" type="checkbox"/> Animals and other organisms
<input checked="" type="checkbox"/>	<input type="checkbox"/> Human research participants
<input checked="" type="checkbox"/>	<input type="checkbox"/> Clinical data
<input checked="" type="checkbox"/>	<input type="checkbox"/> Dual use research of concern

n/a	Involved in the study
<input checked="" type="checkbox"/>	<input type="checkbox"/> ChIP-seq
<input type="checkbox"/>	<input checked="" type="checkbox"/> Flow cytometry
<input checked="" type="checkbox"/>	<input type="checkbox"/> MRI-based neuroimaging

## Antibodies

Antibodies used	<ol style="list-style-type: none"> <li>1. Rabbit anti-GFP, 1:5000 (Thermo Fisher, A11122)</li> <li>2. mouse anti-Arl13b, 1:1000 (Antibodies Inc, 75-287)</li> <li>3. mouse M1 FLAG antibody, 1:1000 (generated in-house)</li> <li>4. Rabbit anti-PKA-C, 1:1000 (generated in-house, for peptide arrays)</li> <li>5. rabbit anti-GST antibody (antibody amount = 8000 RU, as assessed via online SPR measurements) (Carl Roth, 3998.1)</li> <li>6. Rabbit monoclonal anti-Engrailed (Monoclonal Antibody Facility, Institute of Neuroscience, University of Oregon, catalog #4D9)</li> <li>7. mouse polyclonal anti-Prox1 (AngioBio, 11-002P)</li> <li>8. mouse anti-PKA-C, 1:200 (BD, 610981, for imaging studies)</li> <li>9. mouse anti-V5 antibody, 1:1000 (R960-25, Thermo Fisher)</li> </ol>
Validation	<ol style="list-style-type: none"> <li>1. Validated using immunoblot of HEK293 lysates heterologously expressing GFP- or YFP-tagged proteins.</li> <li>2. Validated via Western blot (lysate from control vs Arl13b knockout fibroblasts)</li> <li>3. Validated via FACS, immunofluorescence (control vs. transfected HEK293 using FLAG-tagged protein)</li> <li>4. Validated using purified recombinant PKA-C<math>\alpha</math> (used here as a detection reagent for in vitro systems where no other proteins are present)</li> <li>5. Validated using Western blot with dilution series of recombinant GST-tagged protein, and for SPR using blank immobilization runs without GST-tagged proteins</li> <li>6. Validated using immunostaining of zebrafish embryos at different stages of development when Engrailed is or is not expressed</li> <li>7. Validated using immunostaining of zebrafish embryos at different stages of development when Prox1 is or is not expressed</li> <li>8. Validated using immunoblot analysis on HeLa cell lysates, as well as purified recombinant proteins (see Walker-Gray et al, PNAS)</li> </ol>

## Eukaryotic cell lines

Policy information about [cell lines](#)

Cell line source(s)	1. HEK293-Freestyle: Thermo Fisher Scientific 2. HEK293FT: Thermo Fisher Scientific 3. IMCD3 Flp-in: gift from P. Jackson, Stanford University 4. Smo <sup>-/-</sup> MEFs: gift from P. Beachy, Stanford University 5. Sf9 cells; gift from K.C. Garcia, Stanford University 6. HEK293 Flp-in T-rax: gift from D. Julius, UCSF 7. NIH3T3 Flp-in: gift from R. Rohatgi, Stanford University
Authentication	None of the cell lines were authenticated
Mycoplasma contamination	Cells are tested annually for mycoplasma contamination (MycoAlert Mycoplasma Detection Kit, Lonza), and all tested negative.
Commonly misidentified lines (See <a href="#">ICLAC</a> register)	no commonly misidentified cell lines were used

## Animals and other organisms

Policy information about [studies involving animals](#); [ARRIVE guidelines](#) recommended for reporting animal research

Laboratory animals	Zebrafish ( <i>Danio rerio</i> ), both sexes used, embryonic stages only (exactly 26 hours post-fertilization (hpf))
Wild animals	No wild animals were used in this study.
Field-collected samples	No field collected samples were used in this study.
Ethics oversight	Zebrafish <i>D. rerio</i> were maintained in accordance with approved institutional protocols at the University of Utah. Specifically, all experimental protocols received ethical approval from the University of Utah Institutional Animal Care and Use Committee and were in accordance with the guidelines from the National Institutes of Health (Approval number: 19–11006).

Note that full information on the approval of the study protocol must also be provided in the manuscript.

## Flow Cytometry

### Plots

Confirm that:

- The axis labels state the marker and fluorochrome used (e.g. CD4-FITC).
- The axis scales are clearly visible. Include numbers along axes only for bottom left plot of group (a 'group' is an analysis of identical markers).
- All plots are contour plots with outliers or pseudocolor plots.
- A numerical value for number of cells or percentage (with statistics) is provided.

### Methodology

Sample preparation	HEK293 suspension cells
Instrument	Beckman Coulter Cytotflex
Software	CytExpert 2.3.1.22 (acquisition) FlowJo 10.8.1 (analysis)
Cell population abundance	No cell sorting was performed during our experiments
Gating strategy	Gating was performed for forward and side scatter only

Tick this box to confirm that a figure exemplifying the gating strategy is provided in the Supplementary Information.